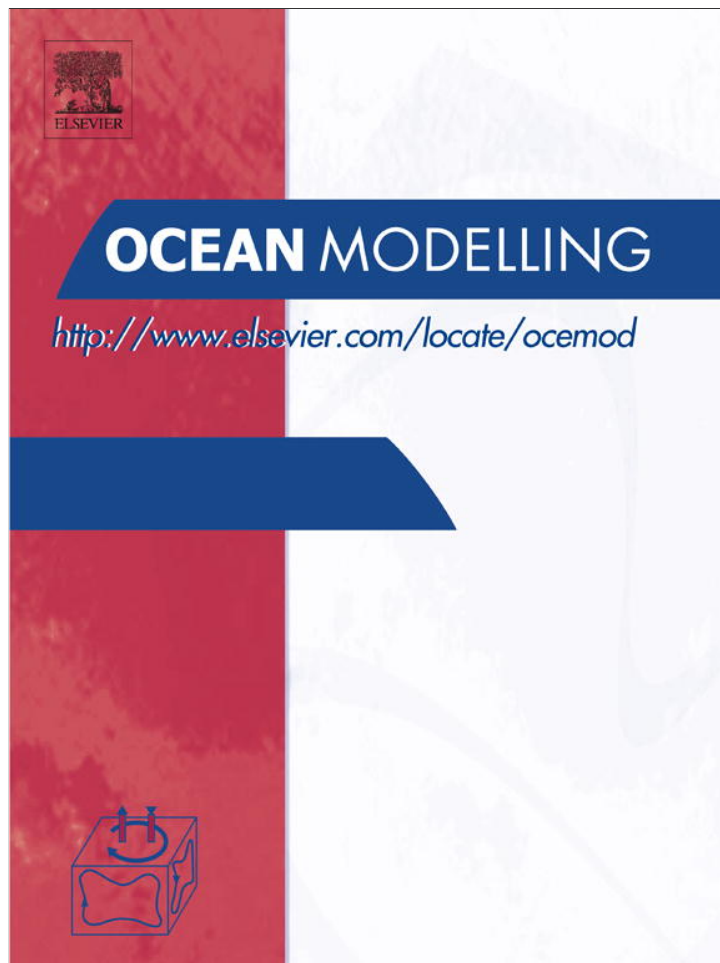


Provided for non-commercial research and education use.  
Not for reproduction, distribution or commercial use.



(This is a sample cover image for this issue. The actual cover is not yet available at this time.)

This article appeared in a journal published by Elsevier. The attached copy is furnished to the author for internal non-commercial research and education use, including for instruction at the authors institution and sharing with colleagues.

Other uses, including reproduction and distribution, or selling or licensing copies, or posting to personal, institutional or third party websites are prohibited.

In most cases authors are permitted to post their version of the article (e.g. in Word or Tex form) to their personal website or institutional repository. Authors requiring further information regarding Elsevier's archiving and manuscript policies are encouraged to visit:

<http://www.elsevier.com/copyright>



ELSEVIER

Contents lists available at SciVerse ScienceDirect

## Ocean Modelling

journal homepage: [www.elsevier.com/locate/ocemod](http://www.elsevier.com/locate/ocemod)

## On multi-scale dispersion under the influence of surface mixed layer instabilities and deep flows

Tamay M. Özgökmen<sup>a,\*</sup>, Andrew C. Poje<sup>b</sup>, Paul F. Fischer<sup>c</sup>, Hank Childs<sup>d</sup>, Harinarayan Krishnan<sup>d</sup>, Christoph Garth<sup>e</sup>, Angelique C. Haza<sup>a</sup>, Edward Ryan<sup>a</sup>

<sup>a</sup>RSMAS, University of Miami, FL, USA

<sup>b</sup>Department of Mathematics, College of Staten Island, NY, USA

<sup>c</sup>Math. and Computer Sci. Division, Argonne National Laboratory, IL, USA

<sup>d</sup>Lawrence Berkeley National Laboratory, CA, USA

<sup>e</sup>University of Kaiserslautern, Germany

### ARTICLE INFO

#### Article history:

Received 29 February 2012

Received in revised form 28 June 2012

Accepted 27 July 2012

Available online 13 August 2012

#### Keywords:

Transport

Lagrangian sampling

LES

### ABSTRACT

A series of large eddy simulations is used to assess the transport properties of multi-scale ocean flows. In particular, we compare scale-dependent measures of Lagrangian relative dispersion and the evolution of passive tracer releases in models containing only submesoscale mixed layer instabilities and those containing mixed layer instabilities modified by deeper, baroclinic mesoscale disturbances. Visualization through 3D finite-time Lyapunov exponents and spectral analysis show that the small scale instabilities of the mixed layer rapidly lose coherence in the presence of larger-scale straining induced by the meso-scale motion. Eddy diffusivities computed from passive tracer evolution increase by an order of magnitude as the flow transitions from small to large scales. During the time period when both instabilities are present, scale-dependent relative Lagrangian dispersion, given by the finite-scale Lyapunov exponent ( $\lambda$ ), shows two distinct plateau regions clearly associated with the disparate instability scales. In this case, the maximum value of  $\lambda$  over the submesoscales at the surface flow is three times greater than  $\lambda$  at the mixed layer base which is only influenced by the deeper baroclinic motions. The results imply that parameterizations of submesoscale transport properties may be needed to accurately predict surface dispersion in models that do not explicitly resolve submesoscale turbulent features.

© 2012 Elsevier Ltd. All rights reserved.

## 1. Introduction

### 1.1. Motivation

Many of the most important practical applications of ocean models involve predicting the transport of coastal pollutants, oil spills, biogeochemical tracers, drifting acoustic sensors and mines. In these cases, the predictive skill of a model depends almost entirely upon the spatio-temporal accuracy of the modeled velocity fields. Satellite data assimilation can result in approximately realistic representation of the phase and speed of the model mesoscale features. Recent developments in our understanding of transport in time-dependent flows indicate that the slow-time variability of long-lasting features such as mesoscale eddies and jets are critical to the computation of so-called Lagrangian Coherent Structures (LCS, Haller, 2002; Shadden et al., 2005) which delineate regions of chaos and barriers to transport. In fact, satellite ocean images of sea surface temperature (SST) and ocean color have stimulated

development of techniques to assimilate Lagrangian quantities analogous to LCS to improve modeled velocity fields (Titaud et al., 2011).

Nevertheless, satellite images<sup>1</sup> also indicate that there is an explosion of flow instabilities at scales below the radius of deformation. A particular example was noted from MODIS SST data during the Lateral Mixing (LATMIX) cruise in May–June 2011 in the Gulf Stream region (Fig. 1). Entrainment of a warm filament from the Gulf Stream along the periphery of a cyclonic eddy with a diameter of approximately 150–200 km resulted in the growth of sinusoidal features with a wavelength of 10–20 km (Fig. 1a–c). These features evolved quickly, changing shape during 6-hourly satellite image updates and disappearing completely after about three weeks of their onset (Fig. 1d). This was by no means an isolated event. Similar phenomena were observed several other times during the two month observation period as permitted by cloud cover and the 1 km pixel resolution of MODIS sensors.

These types of motions, with spatial scales ranging from  $O(100)$  m to  $O(10)$  km and evolution time scales of a few days, are

\* Corresponding author. Tel.: +1 305 421 4053.

E-mail address: [tozgekmen@rsmas.miami.edu](mailto:tozgekmen@rsmas.miami.edu) (T.M. Özgökmen).

<sup>1</sup> [http://oceancolor.gsfc.nasa.gov/cgi/image\\_archive.cgi?c=CHLOROPHYLL](http://oceancolor.gsfc.nasa.gov/cgi/image_archive.cgi?c=CHLOROPHYLL).

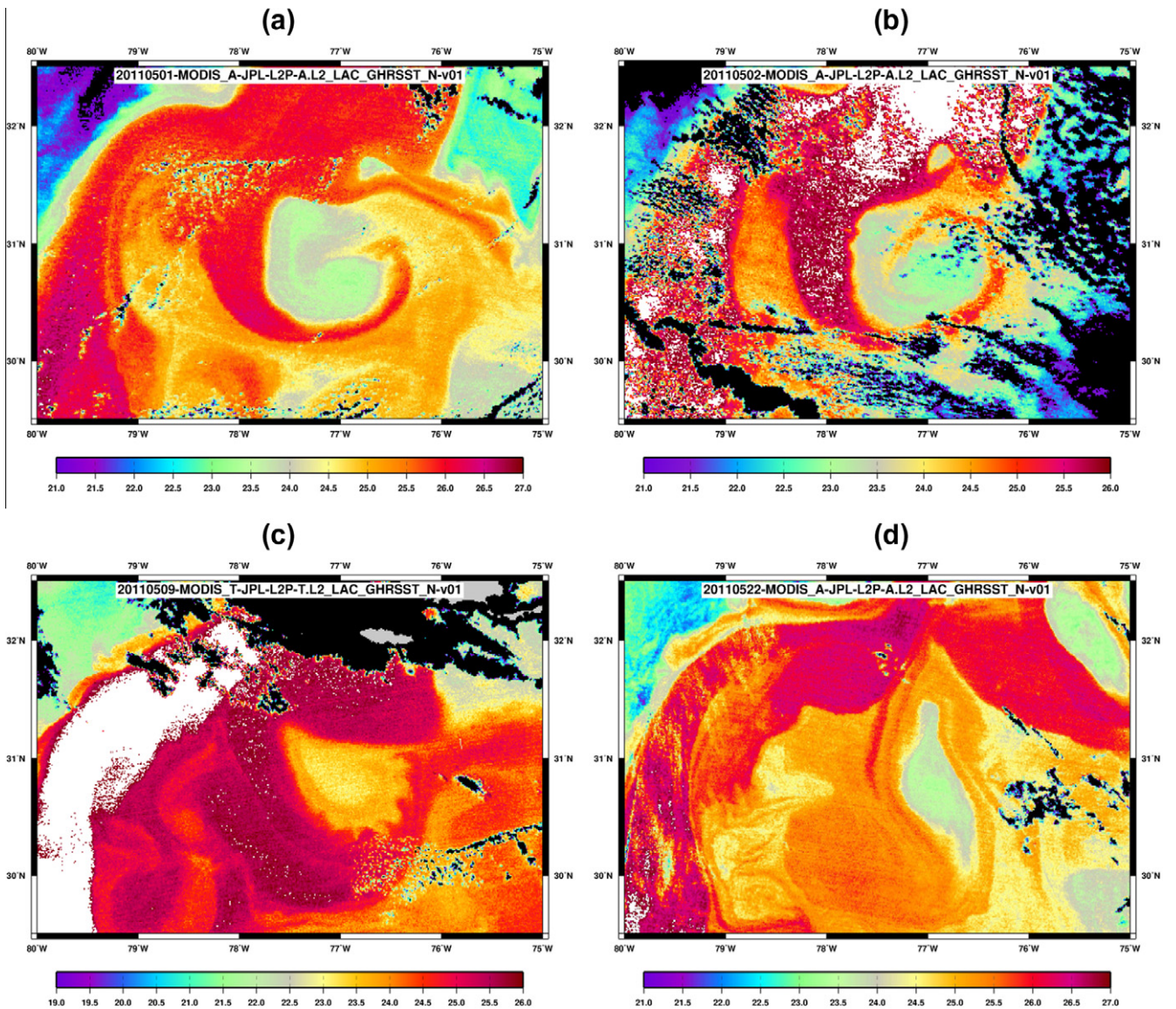


**Fig. 1.** An example of submesoscale instabilities from MODIS SST images in the Gulf Stream region during the LATMIX cruise. (a) Entrainment of a warm filament around a cyclonic eddy,  $t = 0$  (May 1, 2011). (b) The onset what appears to be mixed layer instabilities at  $t = 1$  day. (c) Formation of sinusoidal perturbations along the rim of the cyclonic eddy at  $t = 2$  days. (d) The state of the eddy at  $t = 22$  days.

generally referred to as submesoscale flows (McWilliams, 1985) and have received considerable interest in the recent literature (Mahadevan and Tandon, 2006; Boccaletti et al., 2007; Fox-Kemper et al., 2008; Thomas et al., 2008; Capet et al., 2008a; Mahadevan et al., 2010). This interest is driven in part by fundamental questions concerning the nature of the ocean's energy cascade; namely how do apparently stable mesoscale motions dissipate energy to the smallest scales, and how mesoscale and submesoscale features coexist and interact (Müller et al., 2005; McWilliams, 2008; Klein and Lapeyre, 2009). Given the difficulties involved in both observing and computing flow instabilities and features at widely disparate ocean scales, questions also arise concerning whether the integrated effects of rapidly-evolving and short-lived motions at scales below the radius of deformation  $R_d$  significantly impact mesoscale transport processes.

## 1.2. Theoretical background on relative dispersion

Questions on transport are best addressed in the Lagrangian framework

$$\frac{d\mathbf{r}}{dt} = \mathbf{v}(t) = \mathbf{u}(\mathbf{x}, t), \quad (1)$$

where  $\mathbf{r}$  is the space vector,  $\mathbf{v}(t)$  is the temporal evolution of the Lagrangian velocity vector of a particle along its trajectory and  $\mathbf{u}(\mathbf{x}, t)$  is the corresponding Eulerian velocity field.

Following Poje et al. (2010), and denoting the trajectory by  $\mathbf{x}(\mathbf{a}, t)$  where  $\mathbf{x}(\mathbf{a}, t_0) = \mathbf{a}$ , the relative separation of a particle pair is given by  $\mathbf{D}(t, \mathbf{D}_0) = \mathbf{D}_0 + (\mathbf{x}(\mathbf{a}_1, t) - \mathbf{x}(\mathbf{a}_2, t)) = \mathbf{D}_0 + \int_{t_0}^t \delta\mathbf{v}(t', \mathbf{D}_0) dt'$  where the Lagrangian velocity difference is defined by  $\delta\mathbf{v}(t, \mathbf{D}_0) = (\mathbf{v}(\mathbf{a}_1, t) - \mathbf{v}(\mathbf{a}_2, t))$ . Statistical quantities of interest are the relative dispersion  $D^2(t)$  and relative diffusivity  $K(t)$ ,

$$D^2 = \langle \mathbf{D} \cdot \mathbf{D} \rangle \quad \text{and} \quad K(t) = \frac{1}{2} \frac{dD^2}{dt} = \langle \mathbf{D}(t, \mathbf{D}_0) \cdot \delta\mathbf{v}(t, \mathbf{D}_0) \rangle, \quad (2)$$

where  $\langle \cdot \rangle$  is the average of over all particle pairs. Eq. (2) is equivalent to

$$K(t) = 2 \int_{t_0}^t \langle \mathbf{v}(\mathbf{a}, t) \cdot \mathbf{v}(\mathbf{a}, t') \rangle_a dt' - 2 \int_{t_0}^t \langle \mathbf{v}(\mathbf{a}_1, t) \cdot \mathbf{v}(\mathbf{a}_2, t') \rangle dt' + \langle \mathbf{D}_0 \cdot \delta\mathbf{v}(t, \mathbf{D}_0) \rangle. \quad (3)$$

The relative diffusivity is then the sum of three contributions. The first term on the right hand side of Eq. (3) is simply twice the absolute diffusivity of individual trajectories given by the single particle Lagrangian velocity auto-correlation,  $\langle \cdot \rangle$  denotes averaging over particle pairs, and  $\langle \cdot \rangle_a$  over single particles. The second term is the cross-correlation of pair velocities. The third term, the correlation between initial pair separation and velocity differences, is expected to decay in time as particles lose memory of their initial state.

The asymptotic behavior of the relative dispersion for small and large times is well established (Batchelor, 1952; Babiano et al., 1990; LaCasce, 2008). For short times, the velocity difference of particles that are initially close is approximately constant and  $D^2(t) \sim t^2$  while  $K(t)$  grows linearly in time (ballistic regime). For large times (large separation distances), both the second and third terms in Eq. (3) decay to zero as the velocities along each trajectory become uncorrelated.  $K(t)$  becomes constant and the asymptotic growth of  $D^2(t)$  is linear (diffusive regime).

At intermediate time and separation scales where two point velocity statistics are correlated, the question of the behavior of the relative dispersion is less clear, especially in geophysical flows where the effects of rotation and stratification typically lead to the formation of energetic coherent vortex structures. For statistically homogeneous flows, Richardson's regime (Richardson and Apr, 1926),  $D^2 \sim t^3$ , is often observed and is consistent with both the Kolmogorov–Kraichnan inverse energy cascade in 2D turbulence (Batchelor, 1952) and the saturation of two-point Lagrangian-acceleration correlations (Babiano et al., 1990; Castilla et al., 2007). This issue is clarified by Bennett (1984) (see also Castilla et al., 2007; LaCasce, 2008), the scaling of the relative dispersion is related to the local slope of the energy spectrum of the underlying Eulerian velocity field,  $E(k) \sim k^{-\beta}$ , yielding  $D \sim t^{2/(3-\beta)}$  for  $1 < \beta < 3$ , and  $D \sim e^{\lambda t}$  for  $\beta > 3$ . Thus, considering a typical 2D geophysical turbulence kinetic energy spectrum consisting of dual cascade, one expects an exponential regime of the relative dispersion in the enstrophy cascade range of  $\beta = 3$ , while Richardson scaling is obtained in the inverse cascade regime if  $\beta = 5/3$ . The exponential regime is also obtained in the limits of small separation and smooth velocity fields, where  $d\mathbf{D}/dt \sim \nabla \mathbf{u} \cdot \mathbf{D}$  and  $\nabla \mathbf{u}$  is independent of the separation distance, so that  $D \sim e^{\lambda t}$ , with  $\lambda$  being the Lyapunov exponent.

The global averaging operation over all particle pairs in the definition of the relative dispersion does not allow a systematic investigation of the effects of disparate scales of motion on the dispersion statistics. For this purpose, we also consider the finite-scale Lyapunov exponent, FSLE, introduced by Artale et al. (1997) and Aurell et al. (1997):

$$\lambda(\delta) = \frac{\ln(\alpha)}{\langle \tau(\delta) \rangle}. \quad (4)$$

Here  $\langle \tau(\delta) \rangle$  is the average time (over the number of particle pairs) required to separate from a distance of  $\delta$  to  $\alpha\delta$ . The logarithmic relation follows from the limiting case of vanishing initial pair separation in smooth velocity fields, for which the exponential separation rate given by  $\lambda = \ln\{D(t)/D(0)\}/t$  reduces to the classical Lyapunov Exponent as  $t \rightarrow \infty$ . The explicit dependence of the FSLE on the separation scale  $\delta$  allows one to isolate the contribution of dynamics at different space scales to particle separation. FSLE is not only more robust with respect to the average  $D^2(t)$  at large scales that are typically dominated by those particles with largest separations (thus also small pair numbers), but also the FSLE highlights the relative dispersion over the submesoscales. Interestingly, the FSLE appears to be closely related to metrics from information theory in that it is not only a measure of the predictability time of the dynamics at different spatial scales, but also a measure of the degree of

randomness and information content (Gaspard and Wang, 1993; Costa et al., 2005).

The relationship between the regimes of the FSLE and  $D^2$  is readily established (Boffetta et al., 2000). The Richardson regime implies  $\lambda(\delta) \sim \delta^{-2/3}$ , ballistic motion implies  $\lambda(\delta) \sim \delta^{-1}$  and the diffusive regime is given by  $\lambda(\delta) \sim \delta^{-2}$ .

The scale-dependent dispersion laws in the oceanic context are schematically summarized in Fig. 2. For separation scales larger than  $R_d$ , geophysical turbulence leads to Richardson scaling, or in the presence of strong shear flows such as western boundary currents, to ballistic scaling. For  $\delta \gg R_d$ , on the order of the circulation scale, one can expect diffusive scaling associated with uncorrelated pair velocities. Observations from historical datasets of both surface (Davis, 1985; Lacorata et al., 2001) and subsurface (LaCasce and Bower, 2000) Lagrangian measurements clearly show the existence of the diffusive regime at large separation scales where the motion is uncorrelated, while the mesoscale range is typically characterized by a Richardson regime (Ollitrault et al., 2005).

For dispersion in the submesoscale range, the focus of the present investigation, far less is known observationally. Conceptually, one can post two hypotheses:

- Hypothesis-I: The submesoscale field is weak enough to be completely controlled by the mesoscale eddy field and thus does not exert direct influence on particle/tracer transport. This is equivalent to a steep kinetic energy spectrum,  $\beta \geq 3$ , so that  $D \sim e^{\lambda t}$  (with  $\lambda = \lambda_{\max}^I$  in Fig. 2) for  $\delta < R_d$ . In this *non-local* regime (Bennett, 1984), relative dispersion is *scale independent*, resulting from the stretching and folding produced by mesoscale eddies of significantly larger scale.
- Hypothesis-II: If submesoscale processes are energetically important (spectral slope  $\beta < 3$ ), they exert control on relative dispersion at their own scale (*local* regime). Assuming a smallest measurement or dissipation scale of  $\delta_s \approx 10$  m and  $R_d \approx 10^4$  m, classical Richardson scaling of the relative dispersion in the submesoscale regime yields  $\lambda_{\max}^{II}/\lambda_{\max}^I = 10^2$ . A dynamically active submesoscale therefore produces much faster growth of a tracer patch than that expected on the basis of non-local transport. If (and where) Hypothesis-II holds in the ocean, large surface dispersion errors are to be expected in models resolving processes only at the scale  $R_d$ . Hypothesis-II implies a continuous range of scales with sufficiently shallow spectral energy slope, conceptually consistent with an inverse cascade from the submesoscale through the mesoscale. Alternate possibilities exist, namely

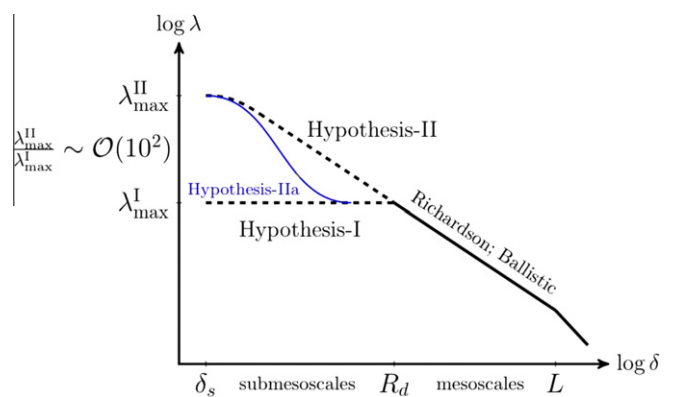
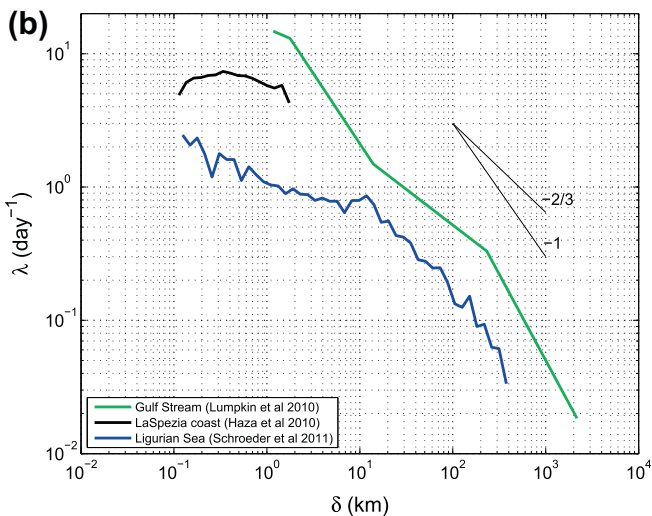
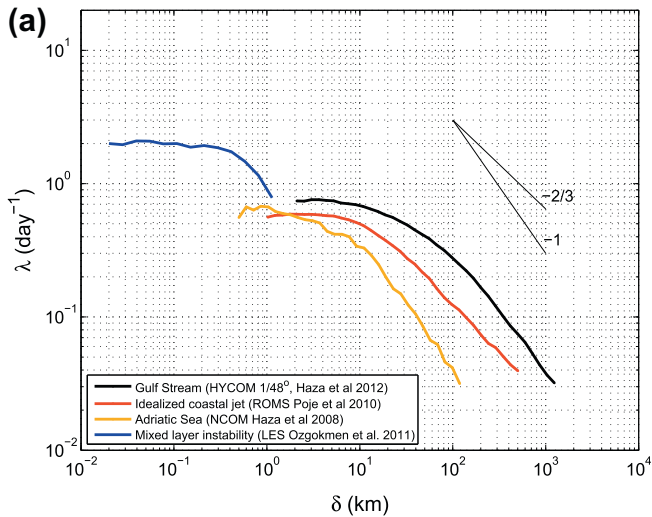


Fig. 2. A schematic depiction of FSLE regimes in the multi-scale setting of the ocean. Hypotheses I & II correspond to non-local and local transport, respectively. Hypothesis-IIa shows a case if there is a significant spectral gap between the submesoscale and mesoscale coherent features inducing the relative dispersion.

the appearance of submesoscale motions produced by mixed-layer instabilities at length scales spectrally distinct from the smallest mesoscale motions. If the spectral gap between the submesoscale and mesoscale is sufficiently large, then scale-dependent dispersion metrics should show two distinct regimes of local transport properties as sketched in the curve labeled Hypothesis-IIa in Fig. 2.

### 1.3. Scale-dependent FSLE in the submesoscale regime

A representative compilation of scale-dependent FSLE,  $\lambda(\delta)$ , from models is shown in Fig. 3a and Table 1. All models show an exponential regime at scales  $\delta \leq R_d$ , with a value of the maximum FSLE,  $\lambda_{max}$ , being in the range of  $0.3 \leq \lambda_{max} \leq 2 \text{ day}^{-1}$ . The magnitude of  $\lambda_{max}$  is found to be given by the strain dominated regions of the flow field (Poje et al., 2010; Haza et al., 2010). In particular, a good correlation was found with positive (hyperbolic) values of  $Q^+ = A^{-1} \int \sqrt{Q} dA$ , for  $Q > 0$ , where  $Q = S^2 - \omega^2 = \left(\frac{\partial u}{\partial x} + \frac{\partial v}{\partial y}\right)^2 + 4\left(\frac{\partial u}{\partial y} \frac{\partial v}{\partial x} - \frac{\partial u}{\partial x} \frac{\partial v}{\partial y}\right)$  is the Okubo–Weiss criterion (Okubo, 1970; Weiss, 1991),  $S^2 = \left(\frac{\partial u}{\partial x} - \frac{\partial v}{\partial y}\right)^2 + \left(\frac{\partial v}{\partial x} + \frac{\partial u}{\partial y}\right)^2$  is the square of the horizontal strain rate,  $\omega^2 = \left(\frac{\partial v}{\partial x} - \frac{\partial u}{\partial y}\right)^2$  the square of horizontal vorticity, and



**Fig. 3.** Scale-dependent FSLE curves from some representative (a) modeling and (b) observational studies. Ballistic ( $\lambda \sim \delta^{-1}$ ) and Richardson ( $\lambda \sim \delta^{-2/3}$ ) regimes are indicated.

$A$  is the sampling area. For instance, using a simple scaling of  $Q^+ \sim \Delta U/R_d$ , and taking as the speed change in the hyperbolic regions  $\Delta U \approx 0.30 \text{ m/s}$ , and  $R_d \approx 50 \text{ km}$  for the Gulf Stream, we get  $\lambda_{max} \approx 0.6 \text{ day}^{-1}$  which falls within the computed range from models. The range of  $\delta$  over the exponential plateau indicates the size of the smallest resolved eddies.

Scale-dependent dispersion results from numerical models which do not explicitly resolve the submesoscale are essentially constrained to be consistent with Hypothesis-I in Fig. 2. They rely on the assumption of smooth, differentiable velocity fields at scales  $\mathcal{O}(2\Delta x)$ . The same holds true for the LES model explicitly resolving the submesoscale. Here there is a well defined plateau in the FSLE at the smallest scales, but the overall domain size is too small to address the role of mesoscale features in transport and stirring. In fact, none of the model-based FSLEs in Fig. 3a results from truly multi-scale simulations; either the mesoscale or the submesoscale eddies are well resolved, but not both together.

A compilation of results from observational studies is given in Table 1 and in Fig. 3b. Even though the world ocean has been extensively sampled by drifters over the past few decades (Lumpkin and Pazos, 2007), the main objective until recently has been to estimate the basin scale mean flow, or local velocity, or single particle diffusivity from individual drifter trajectories. Subsequently, we are aware only of five data sets in which either clusters of drifters at submesoscale initial separations were launched specifically to estimate relative dispersion (Kozalka et al., 2009; Lumpkin and Elipot, 2010; Haza et al., 2010; Schroeder et al., 2011; Berti et al., 2011), or the original data density allowed estimation of relative dispersion at such scales (LaCasce and Ohlmann, 2003). While drifters experience the net effect of almost all scales of motion in the ocean, the resulting  $\lambda(\delta)$  is subject to errors arising from low pair numbers at the submesoscales, even if particles get close enough.

We note that some of the observationally-estimated  $\lambda_{max}$  values are much higher than those from models, sometimes by a factor of up to 20. In particular, Lumpkin and Elipot (2010) estimated  $\lambda_{max} \approx 10 \text{ day}^{-1}$  from drifters launched in the Gulf Stream. These drifters were launched in winter and under strong wind forcing conditions. VHF radar observations in the Gulf of La Spezia also reveal high values within the range of  $4 \text{ day}^{-1} \leq \lambda_{max} \leq 7 \text{ day}^{-1}$  (Haza et al., 2010). This could be due to high strain rates induced by the complex geometry of the Gulf.

Perhaps more noteworthy for the purposes of the present study is the lack of a clear and unique FSLE plateau over the submesoscale range in some observational studies. The finding of Lumpkin and Elipot (2010) is consistent with Hypothesis-II, while Berti et al. (2011) put forward two distinct FSLE plateau, presumably one associated with the mesoscale and the other with the submesoscale eddies.

### 1.4. Objectives

In this study, we seek to capture two different classes of motions through large eddy simulations (LES). The first class of motions is the mixed layer instability (MLI, Boccaletti et al. (2007)), which is a clear mechanism for the direct generation of submesoscale fields. The second class of motions are those of deeper baroclinic flows. Both types of motions can be classified as baroclinic instability converting available potential energy into eddy kinetic energy, with the first one initiated by surface density fronts generated by atmospheric forcing, and the second one by large scale horizontal density gradients at depth. Since these two instabilities are stacked in the vertical direction, with MLI being mainly confined approximately to the mixed layer depth (e.g., Fig. 4a in Özgökmen et al. (2011)), it is not clear a priori how they would interact, and in particular,

**Table 1**  
Comparison of the characteristics of exponential regimes from different observational (top panel) and modeling (bottom panel) studies. Superscript (\*) indicates the estimate from relative dispersion whereas the others from FSLE computation. WAC: (idealized) western Adriatic current, MLI: (idealized) mixed layer instability.

Data/model	Region	$\lambda_{max}$ (day <sup>-1</sup> )	FSLE plateau	Citation
SCULP drifters	Gulf of Mexico	0.3	$\delta < 20$ km	LaCasce and Ohlmann (2003)
SCULP drifters	Gulf of Mexico	0.9	$\delta < 3$ km	LaCasce (2008)
POLEWARD drifters	Nordic Seas	0.5 *	$t < 2$ days	Koszalka et al. (2009)
VHF radar	Gulf of La Spezia	4–7	$\delta < 1$ km	Haza et al. (2010)
CODE drifters	Ligurian Sea	0.7–1.5	$\delta < 10$ km	Schroeder et al. (2011)
CLIMODE drifters	Gulf Stream	10	–	Lumpkin and Elipot (2010)
MONDO drifters	Brazil Current	0.15	$10 \text{ km} < \delta < 100 \text{ km}$	Berti et al. (2011)
		0.6	$0.3 \text{ km} < \delta < 3 \text{ km}$	
NCOM (1 km)	Adriatic Sea	0.6	$\delta < 10$ km	Haza et al. (2008)
ROMS (0.5 km)	WAC	0.7	$\delta < 4$ km	Poje et al. (2010)
HYCOM (8 km)	Gulf Stream	0.4	$\delta < 50$ km	Poje et al. (2010)
HYCOM (2 km)	Gulf Stream	0.7	$\delta < 10$ km	Haza et al. (2012)
NCOM (0.6 km)	Ligurian Sea	1	$\delta < 10$ km	Schroeder et al. (2011)
LES (5 to 50 m)	MLI	0.3–2	$\delta < 1$ km	Özgökmen et al. (2011)

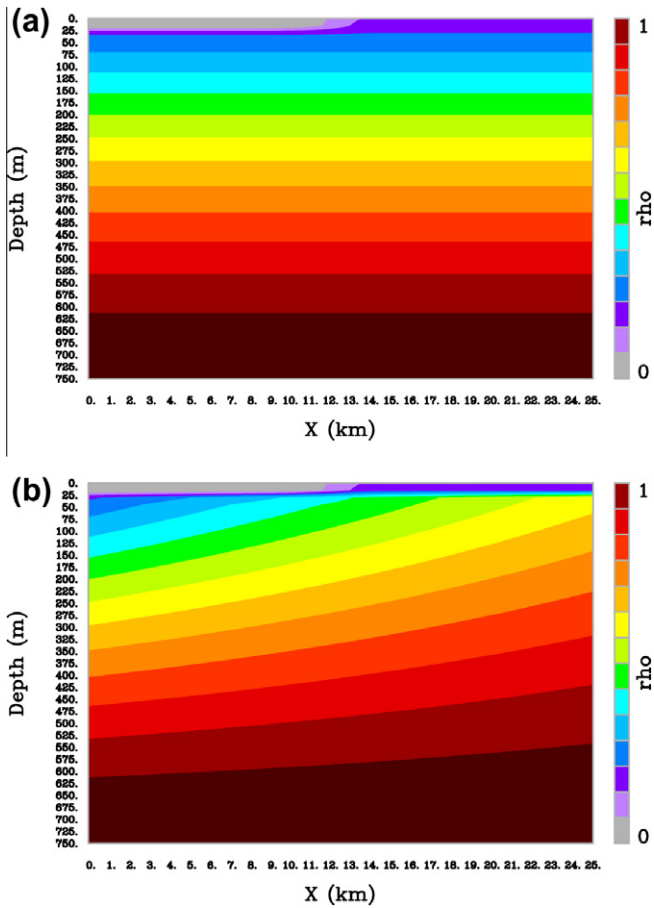


**Fig. 4.** Vertical cross-sections for the density perturbation fields used to initialize (a) Exp-I, and (b) Exp-II.

whether or how deeper instabilities influence the surface transport. In order to minimize aliasing errors that can arise from the rapid evolution of turbulent features, we base our diagnostics on Lagrangian measurements, namely those derived from synthetic particles and tracer fields. The main objective of this study is to determine if and how Hypothesis-II holds true in the computed fields. To our knowledge, this is the first modeling study in which a scale-dependent measure of particle transport is explored in the presence of two, distinct scales of instability.

The paper is organized as follows: The model configuration and the parameters of the numerical experiments are outlined in Section 2. The results presented in Section 3 consist of a description of the flow fields, computation of relative dispersion to explore whether Hypothesis-I or II holds, and an investigation of uncertainties associated with anticipated sampling practices in oceanic experiments. Our principal findings and future directions are summarized in Section 4.

## 2. Numerical methods

### 2.1. Hydrodynamic model configuration and parameters

This numerical study is conducted using Nek5000, which integrates Boussinesq equations based on the spectral element method (Patera, 1984; Maday and Patera, 1989; Fischer, 1997). Nek5000 has been previously used in idealized studies of gravity currents (Özgökmen et al., 2004a; Özgökmen et al., 2004b; Özgökmen et al., 2006; Özgökmen and Fischer, 2008) and these results have formed the basis of refined parameterizations of gravity current mixing for an ocean general circulation model (Chang et al., 2005; Xu et al., 2006). Nek5000 was also employed in studies of exchange flows (Ilicak et al., 2009), the development of subgrid-scale (SGS) models in large eddy simulations (LES) of mixing in stratified flows (Özgökmen et al., 2007; Özgökmen et al., 2009a; Özgökmen et al., 2009b), and most recently, in the investigation of mixed layer instabilities (Özgökmen et al., 2011; Özgökmen and Fischer, in press).

Nek5000 is configured to integrate the non-dimensionalized Boussinesq equations:

$$\begin{cases} \frac{D\bar{\mathbf{u}}}{Dt} = Ro_H^{-1} \hat{\mathbf{z}} \times \bar{\mathbf{u}} - \nabla \bar{p} - Fr^{-2} \hat{\rho}' \hat{\mathbf{z}} + Re^{-1} \nabla^2 \bar{\mathbf{u}} - \nabla \cdot \boldsymbol{\tau}, \\ \nabla \cdot \bar{\mathbf{u}} = 0, \\ \frac{D\bar{\rho}'}{Dt} = Pe^{-1} \nabla^2 \bar{\rho}' - \nabla \cdot \boldsymbol{\sigma}, \end{cases} \quad (5)$$

where the non-dimensional parameters are the Reynolds number  $Re = U_0 H_0 / \nu$ , the Pelet number  $Pe = U_0 H_0 / \kappa$ , the Froude number  $Fr = U_0 / (NH_0)$ , and the vertical Rossby number  $Ro_H = U_0 / (fH_0) = aRo$ , where  $Ro = U_0 / (fL)$  is the Rossby number and  $a = L/H_0$  the ratio of horizontal and vertical domain sizes.  $U_0$  is the flow speed scale,  $H_0$  the total fluid depth,  $\nu$  is the kinematic viscosity,  $\kappa$  is the molecular diffusivity,  $g$  is the gravitational acceleration,  $\rho_0$  is the fluid density,  $N$  is the buoyancy frequency,  $f$  is the Coriolis frequency (a constant here) and  $\hat{\mathbf{z}}$  is the unit vector in the vertical direction.

In (5),  $\frac{D}{Dt} := \frac{\partial}{\partial t} + \bar{\mathbf{u}} \cdot \nabla$  is the material derivative and the variables are considered to be spatially filtered velocity  $\bar{\mathbf{u}} = (\bar{\mathbf{u}}, \bar{\mathbf{v}}, \bar{\mathbf{w}})$ ,

pressure  $\bar{p}$ , and density perturbation  $\bar{\rho}$ . The subgrid scale terms  $\tau = \bar{\mathbf{u}\mathbf{u}} - \mathbf{u}\mathbf{u}$  and  $\sigma = \bar{\mathbf{u}\rho} - \mathbf{u}\rho$ , arise due to spatial filtering with LES. Here, we use the dynamic Smagorinsky SGS model for  $\tau$  and  $\sigma$ . The reader is referred to Özgökmen et al. (2009a); Özgökmen et al. (2009b) for further details.

In addition to (5), two equations related to particle and tracer based sampling strategies are also solved using Nek5000. The first is the advection–diffusion equation for a passive scalar (tracer) field  $C$ :

$$\frac{DC}{Dt} = Pe^{-1} \nabla^2 C. \quad (6)$$

The other is the Lagrangian advection equation for passive, neutrally buoyant particles,

$$\frac{d\mathbf{x}}{dt} = \bar{\mathbf{u}}, \quad (7)$$

where  $\mathbf{x}$  represents the (3D or 2D) time dependent particle position.

The experiment set up is quite similar to that in Özgökmen et al. (2011) and the reader is referred to this paper for brevity here. The model parameters are listed in Table 2. There are two main differences from the study in Özgökmen et al. (2011); the first is the domain size and the second is related to the initial stratification.

The domain size is set to  $L = 25,000$  m in the horizontal and  $H_0 = 750$  m in the vertical directions, respectively. A larger domain than that in Özgökmen et al. (2011) is needed in order to allocate space for the deeper instability that tends to generate larger eddies than by MLI. The domain is discretized using a number of elements of  $K_x = K_y = 32$ ,  $K_z = 8$ . The elements are equally spaced in the horizontal direction and surface intensified in the vertical, as in Fig. 1b of Özgökmen et al. (2011). A polynomial order of  $\mathcal{N} = 13$  is chosen so that the total number of grid points is  $n = (K_x \mathcal{N} + 1)(K_y \mathcal{N} + 1)(K_z \mathcal{N} + 1) = 18,258,345$ . The grid spacing within each element changes according to the distribution of Gauss–Labatto–Legendre quadrature points that are clustered close to the inter-element boundaries to reduce Gibbs oscillations, where the maximum spacing is  $(\Delta x)_{max} \approx \ell \frac{\pi}{2\mathcal{N}}$  and the minimum is  $(\Delta x)_{min} \approx \ell \frac{5}{\mathcal{N}^2}$  for a given element length  $\ell$ . The mesh spacings are  $17 \text{ m} \leq (\Delta x, \Delta y) \leq 94 \text{ m}$  and  $0.75 \text{ m} \leq \Delta z \leq 4 \text{ m}$  (the vertical spacings are listed for the element closest to the upper boundary). The computation time for one model time step scales with  $K_x K_y K_z \mathcal{N}^4$ .

It is important to attain the largest separation between the eddies generated by the MLI and deeper instabilities so that their relative effect on transport can be distinguished. The radius of deformation in the mixed layer is  $R_d^{ML} = \sqrt{\frac{g}{\rho_0} \Delta \rho'_{ML} h_0} / f$  where  $h_0$  is the mixed layer depth and  $\Delta \rho'_{ML}$  is the density change across the surface front. The radius of deformation below the mixed layer is  $R_d = \sqrt{\frac{g}{\rho_0} (\Delta \rho' - \Delta \rho'_{ML})(H_0 - h_0)} / f$ , where  $\Delta \rho'$  is the change across the entire depth. If we assume that the size of the eddies is approximately proportional to these deformation scales, one gets  $R_d / R_d^{ML} = \sqrt{(\Delta \rho' - \Delta \rho'_{ML})(H_0 - h_0) / (\Delta \rho'_{ML} h_0)}$ . Therefore, a weak front in a shallow mixed layer is needed in order to attain a high  $R_d / R_d^{ML}$ .

The mixed layer depth is taken as  $h_0 = 25$  m (thereby,  $(H_0 - h_0) / h_0 = 29$ ), representative of mixed layer depths in the subtropical North Atlantic during the summer season. The initial stratification (Fig. 4) is such that  $(\Delta \rho' - \Delta \rho'_{ML}) / \Delta \rho'_{ML} \approx 3.7$ . As such,

$R_d / R_d^{ML} \approx 10$ ; approximately an order of magnitude scale separation between MLI and deeper eddies is to be expected. Larger scale separation is possible by imposing either shallower and weaker fronts, or by increasing the domain depth, together with the horizontal domain size to accommodate the larger eddies. Both options would require larger computations. All computations have been conducted on 256 processors of a Cray XE6m machine at the City University of New York High-Performance Computer Center<sup>2</sup> and each one took about three days in wall clock time to complete. While it is feasible to conduct larger computations, we could attain our objective with the setup in Fig. 4, as shown in the following.

The study is based on results from two cases. In Exp-I, the deep layers are flat (Fig. 4a) so that only the MLI are permitted in this case. On the other hand, in Exp-II, the deep layers are tilted (Fig. 4b) so that available potential energy can be released through baroclinic instability. The surface front is perturbed along the lateral ( $y$ ) direction by small amplitude sinusoidal perturbations consisting of a superposition of four different wave numbers to facilitate growth of the MLI. Both simulations are started from a state of rest.

## 2.2. Finite-time Lyapunov exponents

Visualization of the turbulent coherent features in a flow field can provide insight into the underlying multi-scale interactions. Temporal evolution of the flow fields can be depicted using 3D plots of  $\rho'$  which effectively help visualize the net effect of turbulent motions on the state of the restratification. However, the dependence of  $\rho'$  on the initial stratification may mask contributions of turbulent coherent structures to the stirring at all scales and, since  $\rho'$  is an active Eulerian quantity, its evolution may not fully reflect the inherent transport pathways of passive tracers in the flow. To this end we also calculate fields of the purely Lagrangian based, short-time finite-time Lyapunov exponents (defined in the following) to visualize transport barriers in the flow field.

In the notation introduced above, Lagrangian transport is described by integral curves  $x$  that are solutions to ordinary differential equation (7). The intuitive understanding associated with integral curves is that of massless particles that are advected through a domain by a vector field  $\mathbf{u}$ . For the category of Lipschitz-continuous vector fields, which are satisfied by the overwhelming majority of applications, existence and uniqueness of solutions to (7) is guaranteed and numerical integration methods can be used to approximate the solution.

In this context, the definition of the finite-time Lyapunov exponents (FTLE) relies on concepts from the theory of dynamical systems; there, the Lyapunov exponent is defined to characterize the rate of separation of infinitesimally close trajectories as time approaches infinity. The idea behind FTLE is to apply this concept in the context of finite-time flow fields and to define a measure of local separation in terms of the trajectories of closely seeded particles.

Considering the position of a particle starting at position  $\mathbf{a}$  at time  $t_0$  after advection along the vector field until time  $t$  can be formulated as the flow map  $x_t(\mathbf{a}, t_0)$ . A linearization of the local variation of this map around the seed position  $\mathbf{a}$  is given by its spatial gradient or Jacobian  $J_t(\mathbf{a}, t_0) := \nabla_{\mathbf{a}} x_t(\mathbf{a}, t_0)$  around  $\mathbf{a}$ . This gradient can be used to determine the maximal dispersion after time  $t_0 - t$  of particles in a neighborhood of  $\mathbf{a}$  at time  $t_0$  as a function of the direction  $dh$  along which one moves away from  $\mathbf{a}$  by considering

$$dh(t) = J_t(\mathbf{a}) dh(t_0). \quad (8)$$

**Table 2**  
Model parameters.

$L$	$H_0$	$Re$	$Pe$	$Fr$	$Ro$
25,000 m	750 m	$10^5$	$7 \times 10^5$	0.1	0.02

<sup>2</sup> <http://www.csi.cuny.edu/cunyhpc/>.

Maximizing  $\|dh(t)\|$  over all possible unit directions  $dh(t_0)$  corresponds to computing the spectral norm of  $J_t$ ; thus, maximizing the dispersion of particles around  $\mathbf{a}$  at  $t_0$  is equivalent to evaluating

$$A_t(\mathbf{a}, t_0) := \sqrt{\lambda^{\max}(J_t(\mathbf{a}, t_0)^T J_t(\mathbf{a}, t_0))}, \quad (9)$$

where  $\lambda^{\max}$  denotes the maximum eigenvalue. To obtain an average exponential separation rate, the logarithm is applied and the result is normalized by advection time to obtain

$$\sigma_t(\mathbf{a}, t_0) := \frac{1}{|t - t_0|} \log(A_t(\mathbf{a}, t_0)). \quad (10)$$

This rate is called the *finite-time Lyapunov exponent* (FTLE), and can be evaluated for both forward-time and backward-time advection. As shown in Shadden et al. (2005) ridges in local extrema fields of  $\sigma$  can be used to extract finite time analogs of stable and unstable hyperbolic manifolds.

To obtain the results presented in the following, 3D FTLE fields are computed on the basis of particles released over half of the domain and integrated forward for two days. Particles are advected using a fifth-order adaptive Runge–Kutta scheme (DOPRI5, cf. Prince and Dormand (1981)) for computational efficiency. The seed points are arranged over a regular grid with a resolution of  $n_x = 501$ ,  $n_y = 251$ ,  $n_z = 51$ , necessitating the computation of 6,413,301 particles in total for each investigated time step. We use central differences to evaluate  $J_t$  in (9).

In addition to the 3D plots of  $\rho'$  and FTLEs, a passive scalar is used. The passive scalar field can provide similarities in visualization to the FTLE, but the tracer field evolves under a complex balance between sharpening of gradients by chaotic advection and smoothing by diffusion (Pierrehumbert, 1994; Pattanayak, 2001; Sundaram et al., 2009), and requires suitable initial conditions.

### 3. Results

#### 3.1. Description of the flow fields

Throughout the entire 173 day evolution, the flow fields in Exp-I are characterized by mixed layer eddies (Fig. 5). These eddies are a few hundred meters in diameter and their vertical extent is confined approximately to the depth of the mixed layer as captured by the FTLE. The restratification is carried out by these eddies and by the propagation of inertia-gravity waves, apparently emitted from the frontal region, across the mixed layer. Since these waves are only marginally resolved in the present model we focus primarily on the eddy-driven turbulent exchange. Very little activity can be observed in deeper ocean, as indicated by almost unperturbed  $\rho' = 0.5$  isopycnal at all times.

The evolution of Exp-II is quite similar to that of Exp-I for approximately the first 100 days of integration, during which MLI act as perturbations to excite the growth of baroclinic instability in deeper layers (Fig. 6a). At  $t = 131$  days the growth of meanders with a wavelength of approximately 8 km is clearly visible (Fig. 6b). While these meanders originate in deeper layers, they have a clear surface signature. The MLI eddies are now imbedded in and transported by these meanders, which we will term *mesoscale* hereafter. The FTLE fields clearly show that MLI stretch under the strain exerted by the mesoscale meanders, losing their vortex structure and creating fine-scale filaments. In addition, the FTLE fields indicate that mesoscale transport barriers begin extending vertically well below the mixed layer base. At  $t = 160$  days, turbulent coherent structures appear to be almost entirely controlled by the mesoscale motions. While the snapshot of the surface density perturbation field still depicts some hints of submesoscale filaments surrounding the mesoscale meanders, the FTLE is almost

entirely free from such structures (Fig. 6c). This indicates that at this stage, the transport is fully dictated by the mesoscale flows. The computation is terminated shortly after the mesoscale flows start interacting with the closed boundaries of the domain (Fig. 6d). At this point in time, mesoscale meanders have generated several coherent eddies with a diameter of roughly 5 km and these structures lack pronounced signs of submesoscale features.

Wave number spectra of kinetic energy  $KE = (u^2 + v^2 + w^2)/2$  are computed on the basis of 201 horizontal surface profiles between the periodic lateral boundaries in the entire domain. The  $KE$  is normalized by the average instantaneous kinetic energy from these profiles. Most of the broad-band perturbations used to initialize the front decay over the first week of the computation (not shown). In the case of Exp-I, there is a clear signal at wave number  $k \approx 1/500 \text{ m}^{-1}$  at  $t = 29$  days (Fig. 7a), which is associated with the formation of submesoscale eddies (Fig. 5a). At  $t = 41$  days, the  $KE$  peak at submesoscales has broadened a bit, giving indications of downward energy cascade. Apparently, this trend is persistent, because we still encounter a sharp  $KE$  peak centered around  $k \approx 1/500 \text{ m}^{-1}$ , as well a new one at  $k \approx 1/250 \text{ m}^{-1}$  at  $t = 102$  days. (Such scales should be explicitly well resolved by the model.) At  $t = 168$  days, the spectra between these two peaks (maybe also scales a few hundred meters larger than 500 m) are replaced by a broad band regime. Slope in this quite narrow wave number regime is not as steep as  $k^{-3}$ . It is consistent with  $k^{-5/3}$  (3D forward energy cascade) or with  $k^{-2}$ . A spectral slope of  $k^{-2}$  was put forward by Capet et al. (2008b) on the basis of simulations of the submesoscale-rich California Current.

The behavior of  $KE$  spectra is different in Exp-II (Fig. 7b). At  $t = 102$  days, when we note the first signs of the emergence of mesoscale meanders (Fig. 6a), there is no  $KE$  peak centered around a narrow wave number. But rather a smooth regime in the range of approximately  $1/2500 \text{ m}^{-1} \leq k \leq 1/250 \text{ m}^{-1}$  with a spectral slope consistent with  $k^{-5/3}$  or  $k^{-2}$  is obtained. Apparently, the submesoscale eddies that emerged in Exp-I can lose their coherence under even small amounts of external strain. At  $t = 131$ , there is no change in the wave number regime of  $1/2500 \text{ m}^{-1} \leq k \leq 1/250 \text{ m}^{-1}$ , but a peak at  $k \approx 1/4000 \text{ m}^{-1}$  emerges consistent with the distinct mesoscale meander in Fig. 6b. At  $t = 160$  days, the spectral slope is approximately  $k^{-3}$  for  $1/4000 \text{ m}^{-1} \leq k \leq 1/250 \text{ m}^{-1}$ . This is a clear indication that the most energetic turbulent features of the flow field now reside at the mesoscales.

In order to investigate the turbulent exchange across the frontal zone carried out by eddies of such different scales, the horizontal second moment of the passive scalar field is computed. Regarding the passive scalar initial conditions, we consider a stream-wise independent form

$$C(\mathbf{x}, t = 0) = \exp\left(-\frac{(x - x_c)^2}{\ell_x^2}\right) \exp\left(-\frac{z^2}{\ell_z^2}\right), \quad (11)$$

where  $x_c = 12,500 \text{ m}$  is at the center of the domain,  $\ell_x = 500 \text{ m}$  and  $\ell_z = 100 \text{ m}$ . While this initial condition amounts to tracer volumes significantly larger than those feasible in oceanic experiments, this volume is necessary to estimate accurately the turbulent frontal exchange given the model resolution. The challenge associated with modeling a realistic amount of tracer release was studied in Özgökmen and Fischer (in press).

We consider the second moment of passive scalar, or its mean square displacement in the  $x$  direction:

$$\sigma_x^2(z_0, t) = \frac{\iint (x - \bar{x}(z_0, t))^2 C(x, y, z_0, t) dx dy}{\iint C(x, y, z_0, t) dx dy}, \quad (12)$$

where integrals are limited by the domain size,  $x$  is the cross-front direction,  $z_0$  m is the depth at which horizontal second moment of

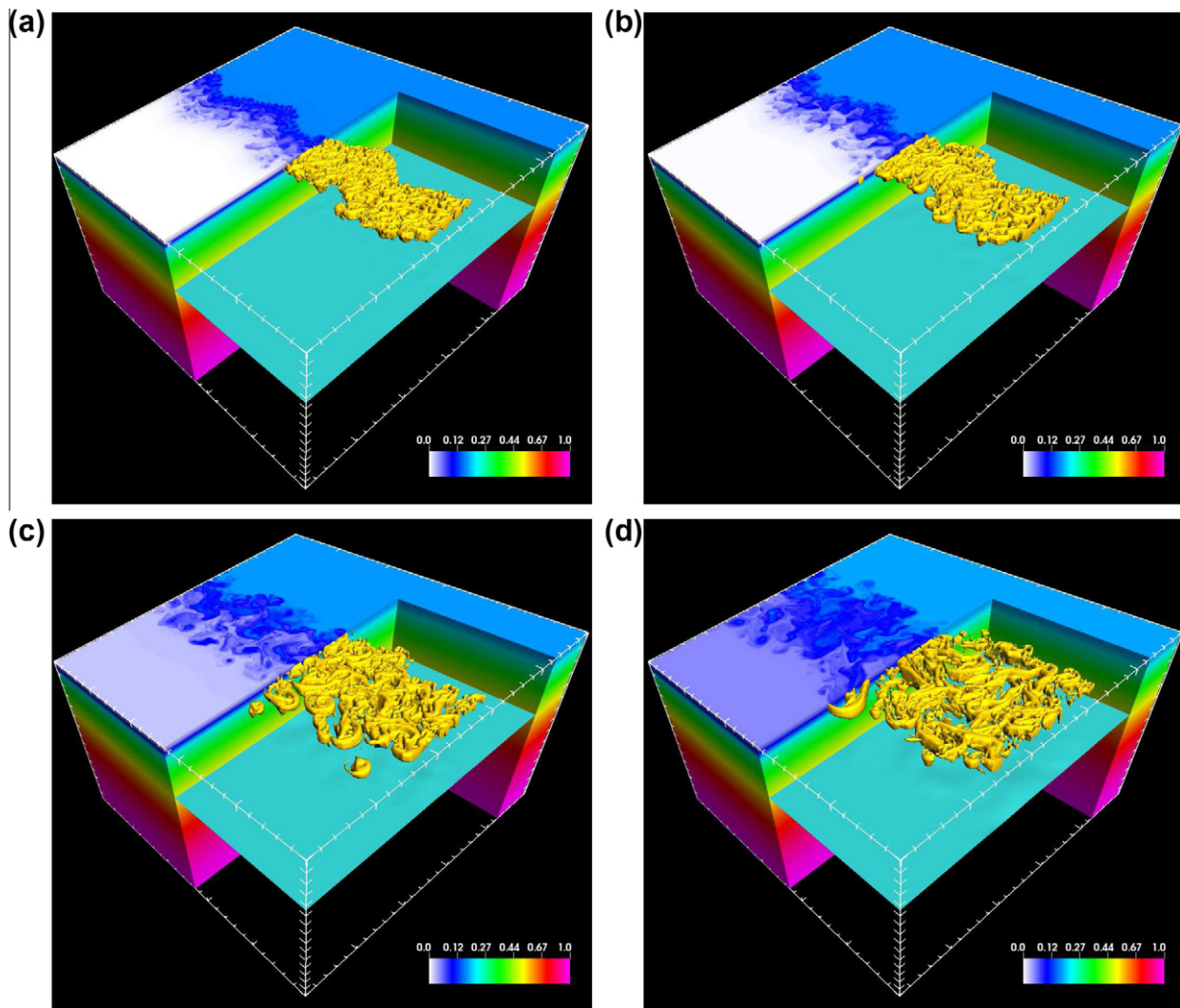


**Fig. 5.** The density perturbation field and FTLEs in Exp-I after (a) 29, (b) 41, (c) 102 and (d) 168 days of initialization. Surfaces corresponding to  $\rho' = 0.5$  (blue) and  $FTLE = 0.33 \text{ day}^{-1}$  (yellow) are shown. The thick marks are placed every 1 km in the horizontal and 50 m in the vertical directions. The animation is available from: <http://www.rsmas.miami.edu/personal/tamay/3D/mlis13.mov>. (For interpretation of color in figures, the reader is referred to the Web version of this article.)

tracer is computed and  $\bar{x}$  is the instantaneous center of mass of tracer distribution,

$$\bar{x}(z_0, t) = \frac{\iint xC(x, y, z_0, t) dx dy}{\iint C(x, y, z_0, t) dx dy}. \quad (13)$$

In Exp-I,  $\sigma_x^2(t)$  grows approximately linearly in time (Fig. 8a). This implies that the spreading of the passive tracer concentration field averaged along the front,  $\bar{C}$ , within the entire mixed layer in  $x$  direction can be described by a normal diffusive process:

$$\frac{\partial \bar{C}}{\partial t} = \kappa_x \frac{\partial^2 \bar{C}}{\partial x^2}, \quad (14)$$

with  $\kappa_x$  being an effective diffusivity that can be extracted from the mean square displacement as (Sundermeyer and Ledwell, 2001)

$$\frac{\partial \sigma_x^2(z_0, t)}{\partial t} = 2\kappa_x(z_0). \quad (15)$$

From Fig. 8a, we obtain for Exp-I,  $\kappa_x \approx 0.25 \text{ m}^2/\text{s}$ . No difference within the mixed layer is observed;  $\sigma_x^2(z_0 = 0 \text{ m}, t) \approx \sigma_x^2(z_0 = 25 \text{ m}, t)$ . The time evolution of  $\sigma_x^2$  in Exp-II is nearly identical to that in Exp-I until about  $t = 80$  days. For  $80 \text{ days} \leq t \leq 120$  days, we observe a slight slow down in the tracer mean square

displacement, which could be because the front cannot continue to expand at its previous pace during the initial formation of the mesoscale meanders. For  $t > 120$  days,  $d\sigma_x^2/dt$  settles to  $10 \text{ m}^2/\text{s}$ , or  $\kappa_x \approx 5 \text{ m}^2/\text{s}$ , namely deep mesoscale eddies enhance the turbulent exchange across the front by 20-fold with respect those carried out by the submesoscale eddies. In regard to comparison of these values to those estimated from ocean measurements, a good agreement is found with diffusivities in the range of  $0.3\text{--}4.9 \text{ m}^2/\text{s}$  estimated from dye releases over a continental shelf (Sundermeyer and Ledwell, 2001).

It is of some interest to explore the sensitivity of tracer mean square displacement estimates to the spatial resolution of the sampling. This is because in ocean experiments, the dye is usually tracked with a single ship and this approach can result in a significant subsampling of the tracer volume. To this end, we have coarsened the mesh spacing over which  $\sigma_x^2$  is computed gradually from  $\Delta x = \Delta y = 100 \text{ m}$  to  $\Delta x = \Delta y = 1000 \text{ m}$ ,  $\Delta x = \Delta y = 2000 \text{ m}$ , and  $\Delta x = \Delta y = 4000 \text{ m}$ . While this is not identical to errors that may result from a vertical profiler tow-yo'd behind a ship traveling at 2–4 kts (Sundermeyer and Ledwell, 2001), it is useful to get some insight into inherent sensitivities of this metric. Overall, we find that  $\sigma_x^2$  is very robust to spatial subsampling (Fig. 8b).

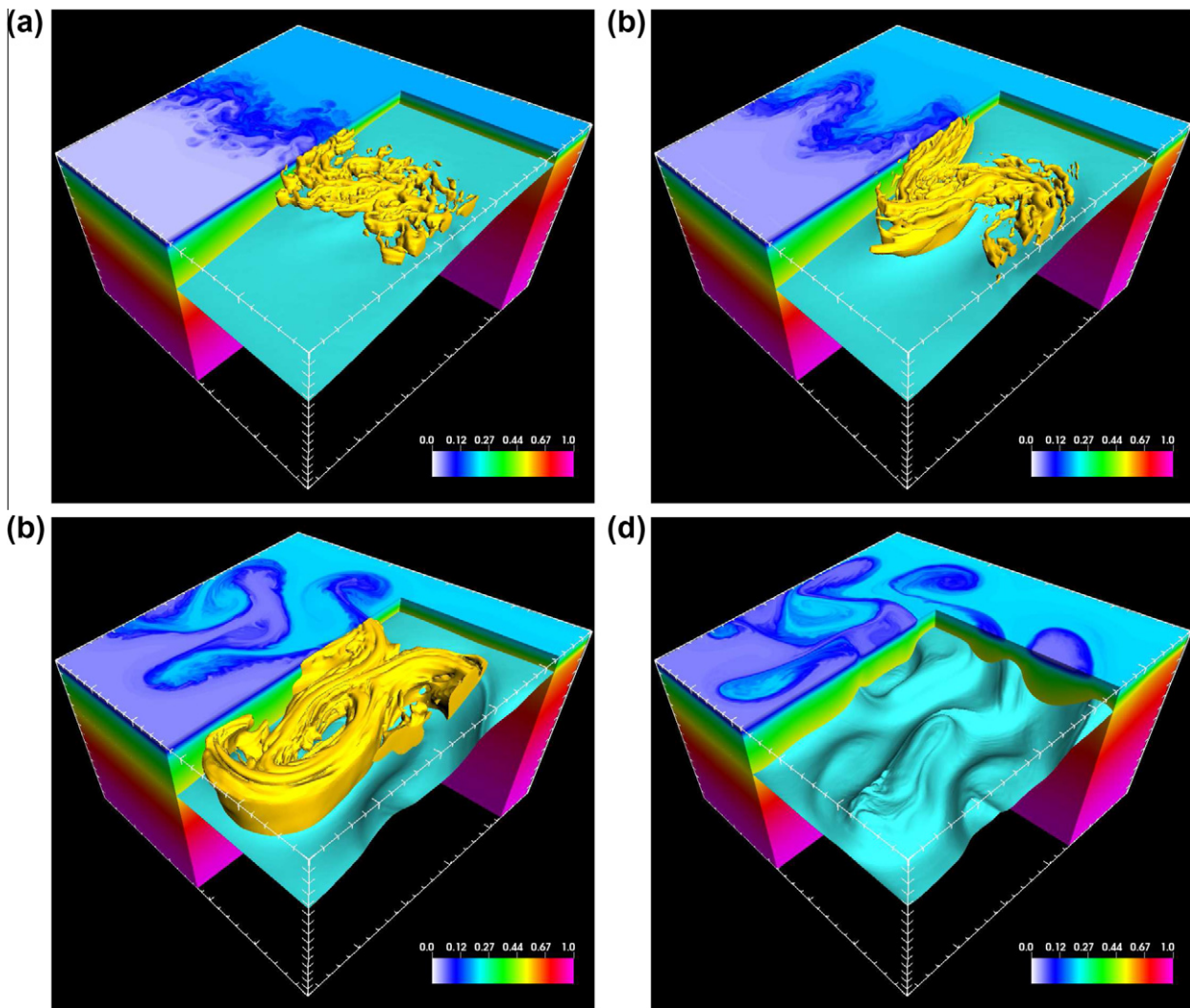


**Fig. 6.** The density perturbation field and FTLEs in Exp-II after (a) 102, (b) 131, (c) 160 and (d) 168 days of initialization. Surfaces corresponding to  $\rho' = 0.5$  (blue) and  $FTLE = 0.33 \text{ day}^{-1}$  (yellow) are shown. The animation is available from: <http://www.rsmas.miami.edu/personal/tamay/3D/mlis11.mov>. (For interpretation of color in figures, the reader is referred to the Web version of this article.)

### 3.2. Relative dispersion

While it is fairly obvious from Figs. 6, 7a and 8a that mesoscale flow ultimately dominates at all depths and the MLI eddies become much less pronounced when surface fronts are strongly coupled with deep mesoscale instabilities, it is not yet clear whether MLI eddies directly contribute to tracer/particle dispersion. Such a signal is best identified during the phase when the flow transitions from the MLI to mesoscale eddy regime, namely when both instabilities coexist. This transition regime can be quantified on the basis of both a visual inspection of Fig. 6 and  $\sigma_x^2(t)$  in Fig. 8a. Broadly speaking, we are then interested in the period 100 days  $\leq t \leq 150$  days, since only MLI exists before, and mesoscale deep baroclinic motions prevail afterwards.

We select a rectangular region with dimensions  $5 \text{ km} \times 5 \text{ km}$  along the front at  $t = 102$  days for both cases to launch the Lagrangian particles (Fig. 9). In choosing the size of the launch area, we not only cover the approximate width of the turbulent frontal zone at that time, but also take into account some practical aspects of oceanic experiments; the fronts should be wide enough to be identified by MODIS SST images, and it should be feasible to launch drifters over such an area within several hours, namely before a portion of the drifters undergo large separations resulting in a

reduction of pair numbers at submesoscale distances. Particles are released in a regular array of 51 triplets in each direction, with inter-particle distances of 20 m within each triplet and the triplets spaced 100 m apart. Particles are released at the top, middle and bottom of the mixed layer at  $z_0 = 0 \text{ m}$ ,  $z_0 = 10 \text{ m}$ , and  $z_0 = 25 \text{ m}$ . A total of  $3 \times 51 \times 51 = 7803$  particles are released at each of the three depth levels for a total of release of 23409 particles. Using all three  $(u, v, w)$  velocity components, Lagrangian particles are advected online (the entire hydrodynamic code was rerun with a time step of 100 s) in order to minimize errors associated with temporal subsampling of the flow field. As discussed by Haza et al. (2008), temporal smoothing of model velocity fields (their Figs. 5, 6) can influence the values of  $\lambda_{max}$  of interest here.

We compute both classical and scale dependent relative dispersion measures but rely mostly on investigating the shape of  $\lambda(\delta)$  given our hypotheses in Fig. 2. The precise definition of the FSLE as given by Eq. (4) requires a choice of which particle pairs to include in the averaging. In simulations where one can efficiently compute trajectories for dense arrays of initial conditions, it is natural to consider separation time statistics only for original pairs, namely particle pairs initially separated by some small distance. To increase the number of pairs at small separation distances for sparse (observational) data sets, one may consider separation times from

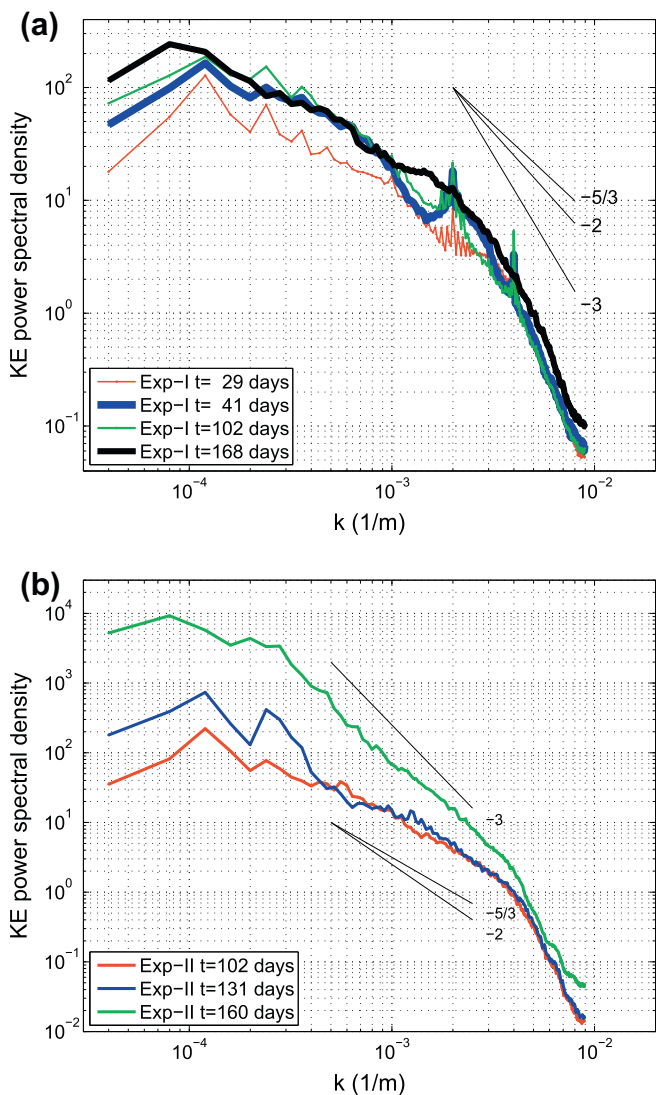


**Fig. 7.** Normalized surface (0 m) kinetic energy power wavenumber spectra for (a) Exp-I after 29, 41, 102 and 168 days, and (b) Exp-II after 102, 131 and 160 days of initialization. Slopes corresponding to  $E \sim k^a$ , with  $a = -3$ ,  $a = -2$  and  $a = -5/3$  are indicated.

so-called chance pairs; any pair of particles separated (at any time) by the given value of  $\delta$ . In the calculation of  $\lambda(\delta)$ , original pairs are used with the full set of drifters, but we resort to chance pairs for estimating  $\lambda(\delta)$  when investigating more realistic drifter numbers. The coefficient in (4) is taken to be  $\alpha = 1.2$  and FSLE is plotted only when pair numbers exceed 10. The reader is referred to Haza et al. (2008); Poje et al. (2010); Haza et al. (2010); Schroeder et al. (2011) for a multitude of sensitivity tests regarding the computation of  $\lambda(\delta)$  from models and ocean data.

The FSLEs at the three levels within the mixed layer in Exp-I are shown in Fig. 10a. The behavior is qualitatively similar to those in our previous study (Özgökmen et al., 2011, their Fig. 11) in that we see Richardson/ballistic type of scaling for  $\delta > 500$  m, the scale of the MLI eddies, and a gradual trend towards FSLE plateau for smaller separation scales. The limiting FSLEs are  $\lambda_{max}(z_0 = 0 \text{ m}) = 0.80 \text{ day}^{-1}$ ,  $\lambda_{max}(z_0 = 10 \text{ m}) = 0.45 \text{ d}^{-1}$ , and  $\lambda_{max}(z_0 = 25 \text{ m}) = 0.27 \text{ day}^{-1}$ .

The results from Exp-II reveal two distinct FSLE plateau in the surface and near-surface  $z_0 = 0 \text{ m}$  and  $z_0 = 10 \text{ m}$  (Fig. 10b) levels. The first plateau exists for  $\delta < 4000 \text{ m}$ , which is consistent with the scale of deep mesoscale eddies, and the other for  $\delta < 400 \text{ m}$ ,

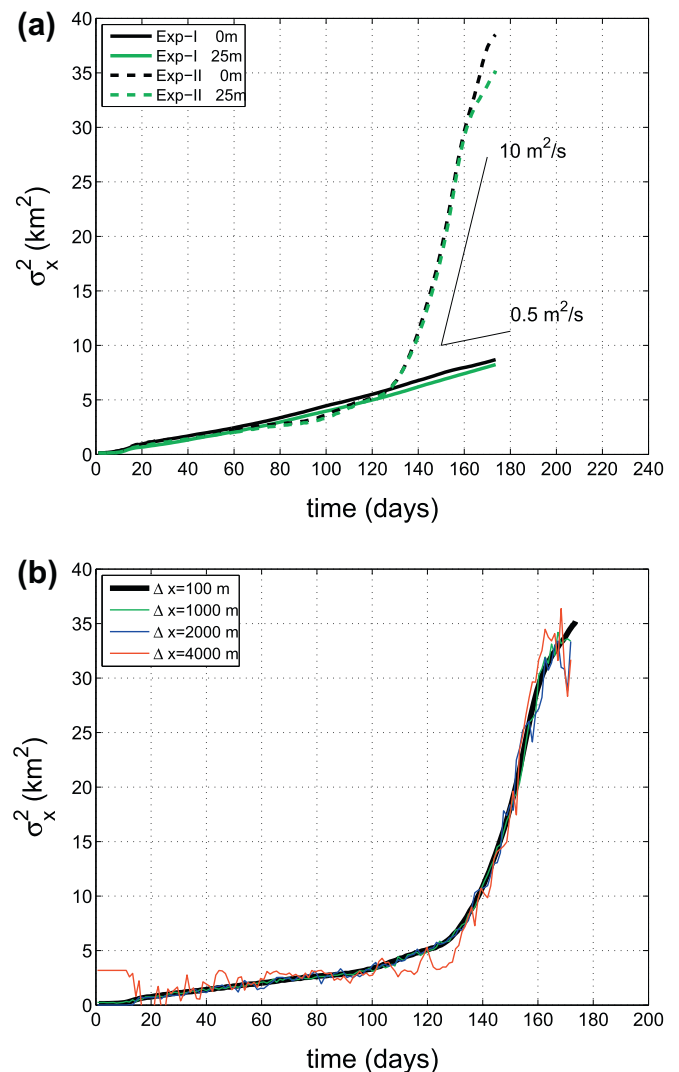


**Fig. 8.** (a) Time evolution of the second moment of passive scalar at depth levels of 0 m and 25 m in Exp-I, and at 0 m, 25 m and 250 m in Exp-II. Slopes corresponding to  $d\sigma_x^2/dt = 0.5$  and  $d\sigma_x^2/dt = 10 \text{ m}^2/\text{s}$  are also shown. (b) Sensitivity of tracer variance estimates at 25 m in Exp-II to spacing of the sampling.

corresponding to mixed layer eddy scale. A single FSLE plateau is observed for particles launched at the mixed layer base,  $z_0 = 25 \text{ m}$ . At this level, MLI eddies are absent and particle transport is the result of deep, mesoscale structures. At separation scales larger than  $\sim 1 \text{ km}$ , the dispersion is completely independent of launch depth clearly indicating that relative dispersion at these scales is entirely determined by the mesoscale field.

The results from Exps. I–II are combined in Fig. 10c by superimposing  $\lambda(\delta, z_0 = 0 \text{ m})$  in Exp-I with  $\lambda(\delta, z_0 = 0 \text{ m})$  in Exp-II and  $\lambda(\delta, z_0 = 25 \text{ m})$  in Exp-II. This figure highlights the fact that  $\lambda_{max}(z_0 = 0 \text{ m})$  in Exp-II is strongly influenced by MLI eddies, while there is a complete collapse of this curve with the one from  $z_0 = 25 \text{ m}$  for  $\delta > 1000 \text{ m}$ , namely for scales at which the influence of MLI eddies on particle separation fade away and that of deeper eddies remain. Given that surface drifters remain confined to  $z = 0$ , the reduction in the peak small-scale values of  $\lambda$  from Exp-I to Exp-II is a direct reflection of the loss of energy of the small-scale MLI structures under deformations by the mesoscale field. The observation of two distinct plateau within the mixed layer, resulting from the dispersive action of two scales of coherent eddies at depth is the primary original accomplishment of this study.

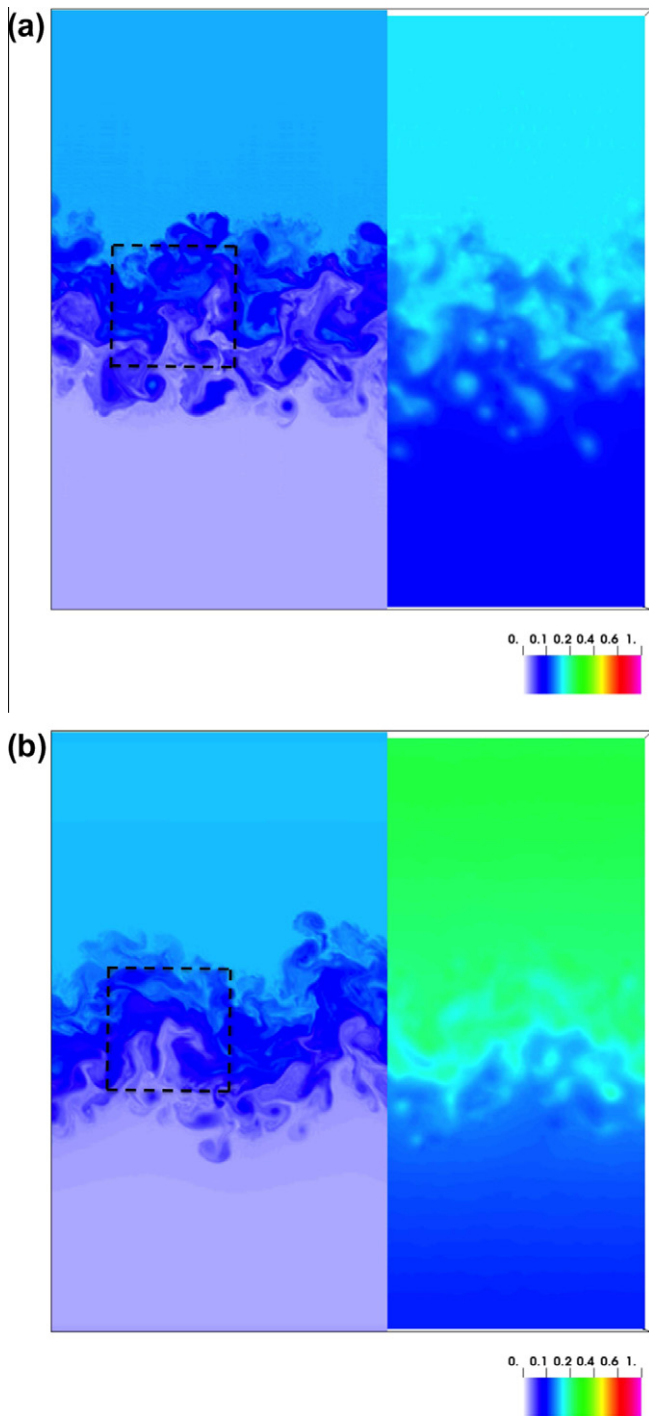


**Fig. 9.** Top view of density perturbation fields at  $t = 102$  days in (a) Exp-I, and (b) Exp-II. The left and right partitions show the fields at depths levels of 0 m and 25 m, respectively. The dashed square marks the region over which particles are launched.

The corresponding effects of energetic submesoscale motions on the traditional relative dispersion metric,  $D^2(t)$ , are shown in 10d. As expected from the FSLE calculations, Exp-II produces significant differences in both the initial growth rate and eventual size of particle patches initialized above and below the mixed layer depth. This difference is clearly attributable to the presence of submesoscale eddies which do not propagate below the mixed layer. In agreement with the FSLE calculations, the presence of mesoscale shearing and strain in Exp-II results in a appreciable reduction in relative dispersion  $D^2(t)$  compared to that observed in Exp-I.

To check the statistics of the FSLE calculation, we estimate the limiting  $\lambda$  by assuming  $D^2(t_2) = D^2(t_1) \exp[2\lambda_D(t_2 - t_1)]$  with  $t_2 > t_1$ . Thereby,  $\lambda_D = \frac{1}{2} \ln\left(\frac{D^2(t_2)}{D^2(t_1)}\right) / (t_2 - t_1)$ . For  $z_0 = 0$  in Exp-I, we select  $t_1 = 102.25$  and  $t_2 = 104.19$  days with  $D^2(t_1) = 0.0005 \text{ km}^2$  and  $D^2(t_2) = 0.0112 \text{ km}^2$  for the exponential regime, while for  $z_0 = 0$  in Exp-II,  $t_1 = 102.42$  and  $t_2 = 105.07$  days with  $D^2(t_1) = 0.0005 \text{ km}^2$  and  $D^2(t_2) = 0.0092 \text{ km}^2$ , and for  $z_0 = 25 \text{ m}$  in Exp-II,  $t_1 = 103.66$  and  $t_2 = 116$  days with  $D^2(t_1) = 0.0005 \text{ km}^2$  and  $D^2(t_2) = 0.0290 \text{ km}^2$  are taken. The comparison of the  $\lambda_{max}$  from the FSLE and  $D^2(t)$  shows excellent agreement (Table 3).

### 3.3. Uncertainty analysis of scale-dependent FSLE

For the purpose of designing real ocean experiments, it is of interest to address the following questions:

- (i) What is the sensitivity of  $\lambda(\delta)$  to the number of Lagrangian particles? In particular, how many particles are needed to get good estimates of  $\lambda(\delta)$ ?
- (ii) What is the length of time needed for sampling? What type of errors result from a reduction of the needed sampling period?
- (iii) Can  $\lambda(\delta)$  errors be reduced by changing the initial launch configuration?

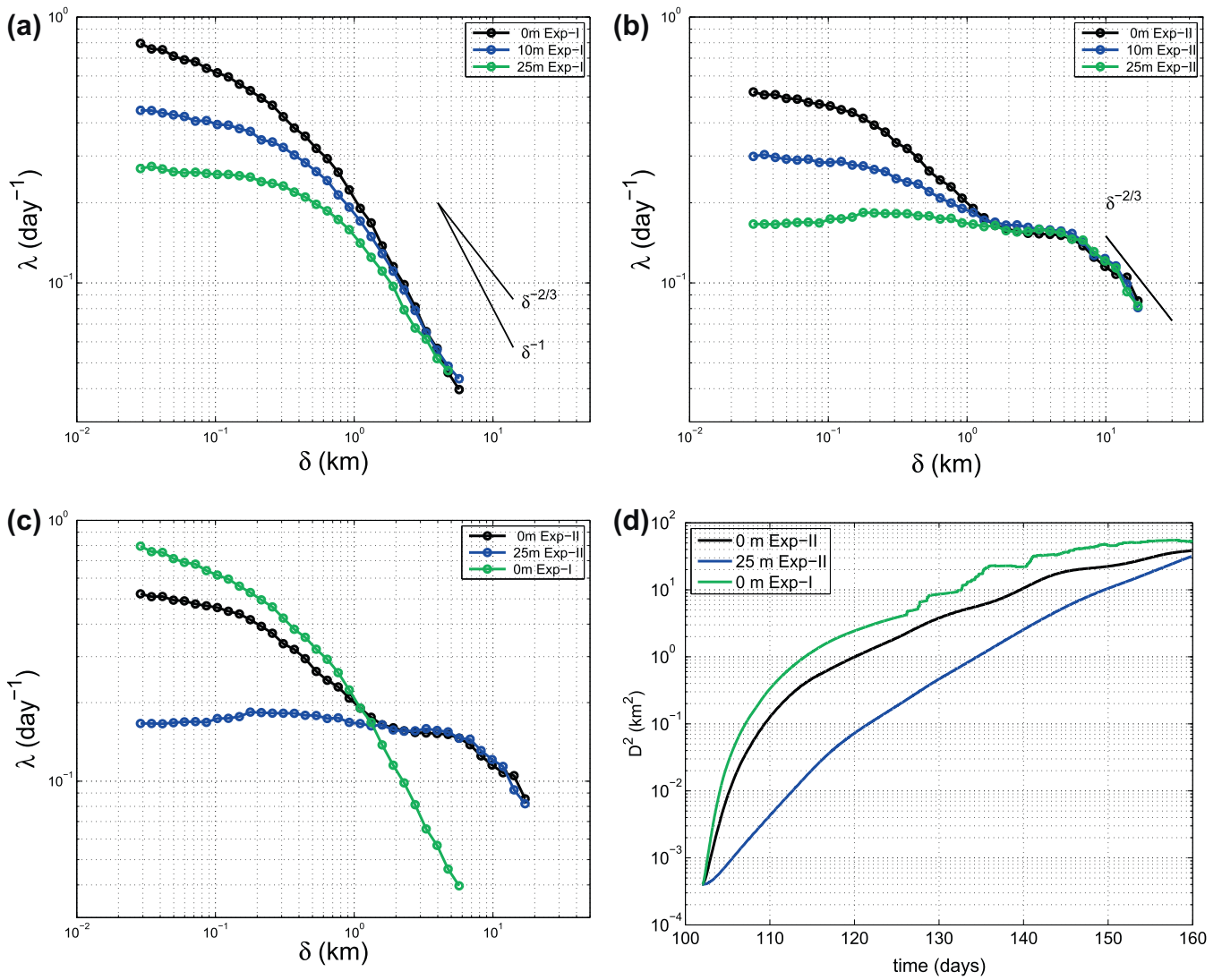
The question (i) is of obvious importance since 7803 drifters are not feasible to deploy in ocean experiments of present time. While (i) was addressed in Özgökmen et al. (2011) within the context of MLI flows, it is not clear whether similar results would hold in the presence of multi-scale instabilities. Question (ii) is also of great practical importance since with 900 s temporal sampling used here, the batteries in commercial drifters last for a maximum of about 15 days.<sup>3</sup> As the testbed to address the issues, flows at  $z_0 = 0 \text{ m}$  in Exp-II are chosen, since two distinct FSLE plateau are obtained in this case.

Fig. 11 shows  $\lambda(\delta)$  curves resulting from 289, 96 and 32 particles integrated for 58 days, as in the case of 7803 particles, which is considered to be the truth. For all these cases with a reduced number of drifters, chance pair calculation is conducted. The results indicate that very consistent estimates of  $\lambda(\delta)$  can be obtained even for 32 drifters. There is a difference by a factor of up to two for  $2 \text{ km} < \delta < 8 \text{ km}$  between the curves obtained from original versus chance pairs. This is similar to what is shown in Fig. 10 of Poje et al. (2010) and it is because the original pair method tends to emphasize the statistics of the fastest separating particles at large  $\delta$ .

Since new and inexpensive drifter designs are likely to make the launch of 96 and 289 drifters a reality in the near future, we focus on these numbers to investigate (ii). The time of integration is reduced from 58 days to 30 and 15 days. Fig. 12 shows that the FSLE plateau associated with submesoscale MLI motions is accurately captured in all cases, while the second mesoscale FSLE plateau is not apparent in any of these cases. By inspecting Fig. 8a, it is seen that a 15-day integration between  $102 \text{ days} \leq t \leq 117 \text{ days}$  is not well placed to sample the onset of dispersion by deep mesoscale eddies. From Fig. 12, one notes again how accurately the FSLE metric provides insight into the scale-dependent dispersive action of the underlying flow field.

Several modifications in the initial launch configuration are then carried out in order to improve the chances of particles for capturing the double FSLE plateau regime. First, the launch time is shifted to  $t = 120$  days, namely nearly to the onset of dispersion driven by deep flows (Fig. 8a). Given the episodic coexistence of

<sup>3</sup> Personal communication with MetOcean, <http://www.metocean.com/>, 2012.



**Fig. 10.** The FSLE  $\lambda(\delta)$  from releases at 0 m (black) 10 m (blue) and 25 m (green) in (a) Exp-I and (b) Exp-II. Superposition of (c) FSLEs and (d) relative dispersion  $D^2(t)$  at 0 m in Exp-I (green), 0 m (black) and 25 m (blue) in Exp-II. (For interpretation of color in figures, the reader is referred to the Web version of this article.)

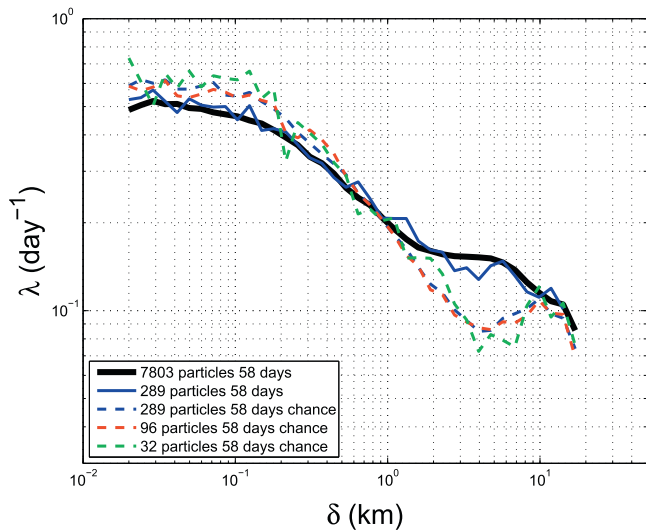


**Fig. 11.** The sensitivity of FSLE  $\lambda(\delta)$  in Exp-II from releases at 0 m to the number of Lagrangian particles.

**Table 3**

Comparison of the limiting  $\lambda$  from FSLE,  $\lambda_{max}$ , and relative dispersion  $\lambda_D$ .

	Exp-I $z_0 = 0$ m	Exp-II $z_0 = 0$ m	Exp-II $z_0 = 25$ m
$\lambda_{max}$ (day <sup>-1</sup> )	0.80	0.52	0.17
$\lambda_D$ (day <sup>-1</sup> )	0.79	0.55	0.16

submesoscale and mesoscale flows, the timing of sampling emerges as one of the primary critical points. Second, the along-front launch distance is increased from 5 km to 10 km, that permits us to cover a wavelength on the scale of mesoscale eddies. Third, the minimum spacing between drifters is increased to 100 m, which is much smaller than the size of submesoscale eddies and allows the growth of separation scales at shorter sampling periods. Finally, drifters are released in pairs as opposed to triplets in order to cover this area using 96 particles.

Under this modified launch strategy, it is found that marginally accurate results displaying both submesoscale and mesoscale FSLE plateau are obtained with 96 particles and 30 days of sampling period (Fig. 13). When the integration period is reduced to 7 days, the mesoscale FSLE plateau is not visible anymore, and at 3 days of observation, there are increased errors for the submesoscale FSLE

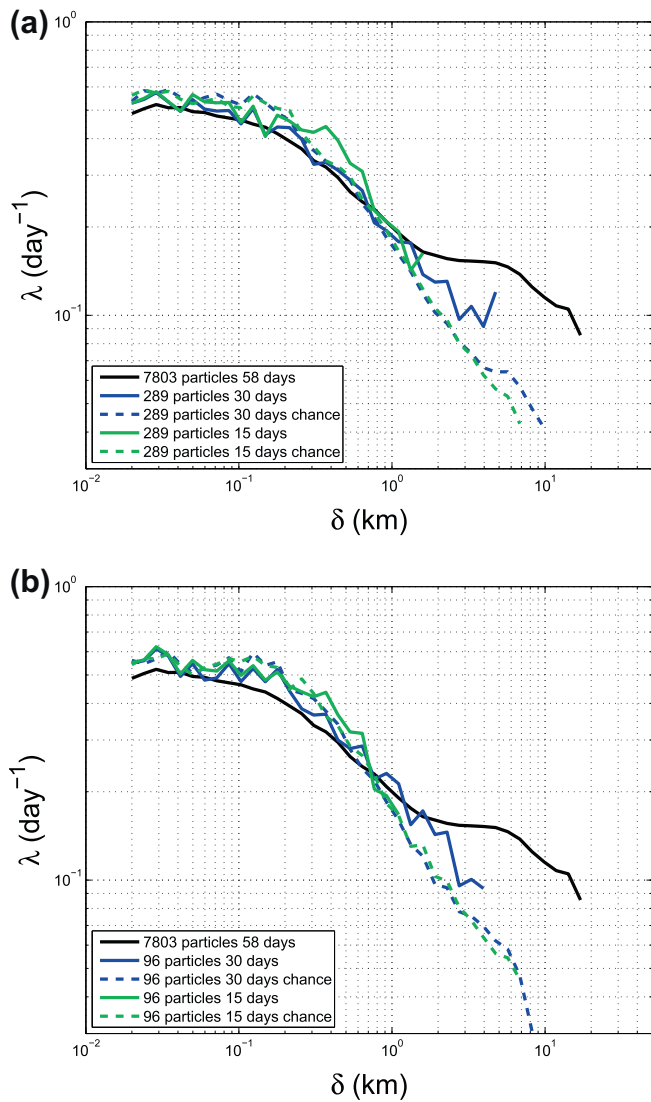


Fig. 12. The sensitivity of FSLE  $\lambda(\delta)$  in Exp-II from releases at 0 m with (a) 289 particles and (b) 96 particles to the length of integration.

plateau. Original pair estimation is more oscillatory than with chance pairs, and extends to smaller separation distances because of lower pair numbers attained.

Overall, we find that a good estimate of the submesoscale FSLE plateau can be obtained from only a few days of Lagrangian particle trajectories. This creates the possibility of launching drifters and retrieving every few days before they disperse beyond the reach of a single ship in order to check the presence of high-strain submesoscale events in the ocean. Nevertheless, an order of magnitude longer observation time is needed to capture the dispersive action of mesoscale features in the flow field, in a clear reflection of the scale separation between these two instabilities. Therefore, both fast-sampling (on the order of 10 min) and long-lasting (on the order of 1–2 months) drifter configurations are needed in ocean observation campaigns in order to resolve transport resulting from both submesoscale and mesoscale events.

#### 4. Summary and conclusions

This study is motivated by a recent observation of the emergence of submesoscale features along the rim of a cyclonic Gulf Stream ring. These submesoscale features developed within days

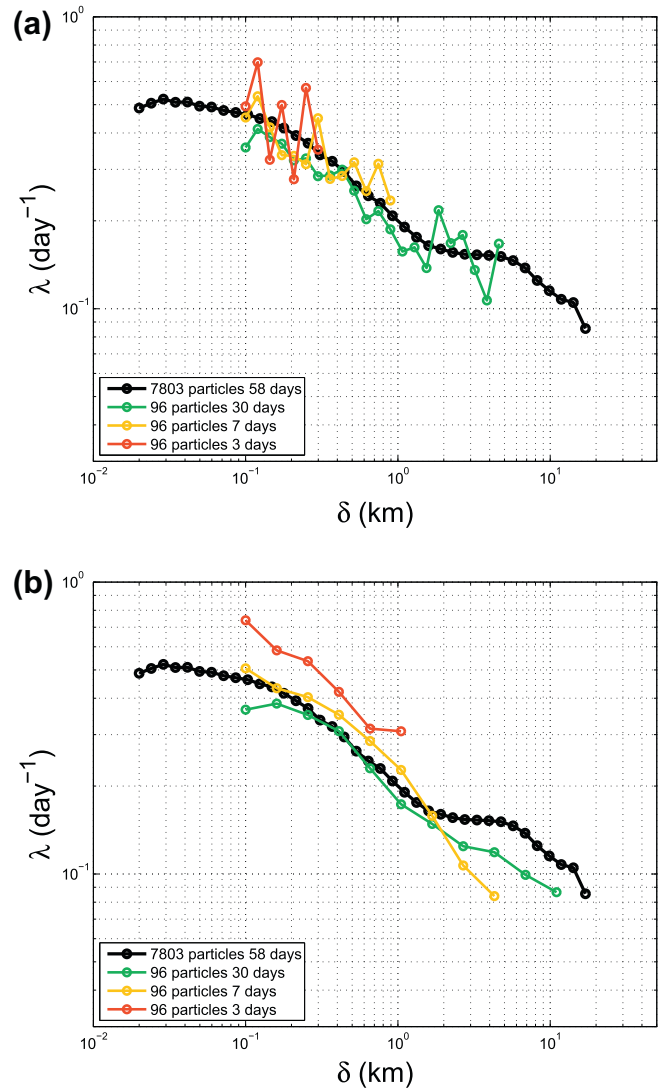


Fig. 13. The sensitivity of FSLE  $\lambda(\delta)$  in Exp-II from releases at 0 m with 96 particles in a modified initial launch to sampling period using (a) original and (b) chance pairs.

after a cyclonic (cold core) ring entrained warm water from the Gulf Stream, but apparently completely dissipated within three weeks of their emergence. Submesoscale features have been notoriously difficult to observe *in situ*, while remote sensing instruments provide occasional glimpses into their structure and rapid evolution. The implication of the multi-scale interaction in this particular case is that submesoscale flows appear sporadically because special circumstances are needed for their formation, and dissipate quickly under the action of mesoscale stirring.

During the time period when both the mesoscale eddy and submesoscale features coexist, the question arises as to which scales control transport. The primary objective of this study is to investigate the validity of two contrasting hypotheses: Hypothesis-I where mesoscale eddies exert non-local control over small scale transport and Hypothesis-II where dispersion and transport at the submesoscales is governed by eddying motions at local scales. The implication of Hypothesis-I is that mesoscale eddy-resolving data-assimilating (current generation) OGCMs would provide adequate predictions in applied important problems such as transport of coastal pollutants and oil spills, while Hypothesis-II would indicate that OGCMs would significantly underestimate the dispersion of a passive pollutant until the patch size grows to the scale of the local radius of deformation. Another complementary objective of

this study is to provide insight into the question of whether and how instabilities below the mixed layer influence surface transport.

LES is used to assess transport properties of multi-scale ocean flows. In particular, the initial density perturbation field is specified in a way that MLI eddies are approximately an order of magnitude smaller than deeper eddies. A parallel experiment is configured for comparison in which the stratification below the mixed layer has no available potential energy, and thereby no independent turbulent coherent structures from the surface motion can form. In particular, we compare scale-dependent measures of Lagrangian relative dispersion and the evolution of passive tracer releases in numerical experiments containing only submesoscale MLI, and MLI modified by deeper, baroclinic mesoscale disturbances.

Visualization of turbulent coherent structures through 3D FTLE and analysis of surface kinetic energy wavenumber spectra show that smaller scale instabilities in the mixed layer rapidly lose their coherence in the presence of larger scale straining induced by mesoscale motions. Tracer-based eddy diffusivity computed to quantify the turbulent exchange across the mixed layer front yields approximately  $\kappa_x \approx 0.25 \text{ m}^2/\text{s}$  uniformly within the mixed layer depth in the case of MLI only, but increases to  $\kappa_x \approx 5 \text{ m}^2/\text{s}$  as the flow transitions to mesoscales. This result is likely to be related to shallow mixed layer depths representative of summer conditions in the North Atlantic. Winter mixed layers are typically an order of magnitude deeper, possibly creating large enough mixed layer eddies that can survive the larger scale straining for long periods.

The scale-dependent FSLE  $\lambda(\delta)$  curves for both cases are computed by releasing 7803 synthetic particles within a 5 km by 5 km square over the front at three levels within the mixed layer. The numerical experiment in which only the MLI is present leads to results consistent with Hypothesis-II, namely a single FSLE plateau emerges at separation scales smaller than the MLI eddies. Given the small length-scales and energy of the MLI eddies, however, the inverse cascade produces a relatively weak mesoscale flow over the limited time period examined. The separation times increase approximately linearly with separation scale for all scales greater than approximately 300 m.

The primary new advance made by this study is that during the period when both MLI and deeper instabilities are present,  $\lambda(\delta)$  at 0 and 10 m depths show two distinct plateaux clearly associated with the disparate instability scales. There is a complete collapse of these curves with the one calculated from particle releases at 25 m for separation distances larger than the scale of MLI eddies ( $\delta > 1000 \text{ m}$ ), indicating that larger scale motions are controlled by deep instabilities. While we do not directly compare flows with and without submesoscale features, the strong effect of such small-scale features on surface transport can be inferred from the significant differences in the dispersion characteristics observed above and below the mixed layer depth in Exp II.

These results indicate the distinct possibility of Hypothesis-II holding, at least episodically, in the upper ocean. For computational reasons, we have examined a situation with two disparate length scales imposed. One could, however, easily imagine multiple mixed layer fronts driven by a range of lateral buoyancy gradients forming eddies of various scales with their mutual interaction creating a nearly continuous spectrum of submesoscale features. Parameterizations to compensate for the dispersion defect between Hypothesis-I and Hypothesis-II for the submesoscales in OGCMs have been put forward recently (Haza et al., 2012).

Given that simultaneous release thousands of drifters is currently not feasible in oceanic experiments, but numbers on the order of one hundred can be readily considered in dedicated studies,

the sensitivity of  $\lambda(\delta)$  is explored to the number of drifters and duration of the trajectories so that both plateaux can be captured. The results indicate that the submesoscale plateau emerges readily with even 32 drifters, while timing and duration are important considerations to reveal both plateaux. Timing is important in that submesoscales do not coexist with mesoscales perpetually while the drifters must sample the flow field long enough to separate under slower evolving mesoscale motions. The results imply that a field experiment would require fast sampling drifters (on the order of minutes) and at least one-month long trajectories to span the scale separation. An implicit assumption made here is that the position error of drifters is negligible with respect to the distance traveled during the sampling intervals. This is a rather severe assumption in light of the existing technology (Ohlmann et al., 2005) and will be subject to a future investigation.

## Acknowledgments

We greatly appreciate the support of the Office of Naval Research and National Science Foundation via Grants N00014-09-1-0267, DMS-1025323, DMS-1025359 (Collaborative Mathematics and Geoscience, CMG, grants) under the Multidisciplinary University Research Initiative (MURI) on Dynamical Systems Theory Ocean 3D + 1 grant. This research was made possible in part by a grant from BP/The Gulf of Mexico Research Initiative. We thank all members of the Lateral Mixing DRI team, who have provided guidance through many insightful discussions. The computations in this research was supported, in part, by a grant of computer time from the City University of New York High Performance Computing Center under NSF Grants CNS-0855217 and CNS-0958379. The authors also thank the two anonymous reviewers whose constructive comments led to a significant improvement of this manuscript.

## References

- Artale, V., Boffetta, G., Celani, A., Cencini, M., Vulpiani, A., 1997. Dispersion of passive tracers in closed basins: Beyond the diffusion coefficient. *Phys. Fluids* 9, 3162–3171.
- Aurell, E., Boffetta, G., Crisanti, A., Paladin, G., Vulpiani, A., 1997. Predictability in the large: an extension of the concept of Lyapunov exponent. *J. Phys. A* 30, 1–26.
- Babiano, A., Basdevant, C., Leroy, P., Sadourny, R., 1990. Relative dispersion in 2-dimensional turbulence. *J. Fluid Mech.* 214, 535–557.
- Batchelor, G.K., 1952. Diffusion in a field of homogeneous turbulence. 2: The relative motion of particles. *Proc. Cambridge Phils. Soc.* 48 (2), 345–362.
- Bennett, A.F., 1984. Relative dispersion – local and nonlocal dynamics. *J. Atmos. Sci.* 41 (11), 1881–1886.
- Berti, S., Santos, F.A.D., Lacorata, G., Vulpiani, A., 2011. Lagrangian drifter dispersion in the Southwestern Atlantic Ocean. *J. Phys. Oceanogr.* 41, 1659–1672.
- Boccaletti, G., Ferrari, R., Fox-Kemper, B., 2007. Mixed layer instabilities and restratification. *J. Phys. Oceanogr.* 37, 2228–2250.
- Boffetta, G., Celani, A., Cencini, M., Lacorata, G., Vulpiani, A., 2000. Nonasymptotic properties of transport and mixing. *Chaos* 1, 50–60.
- Capet, X., McWilliams, J., Molemaker, M., Shchepetkin, A., 2008a. Mesoscale to submesoscale transition in the California Current System. I: Flow structure, eddy flux and observational tests. *J. Phys. Oceanogr.* 38, 29–43.
- Capet, X., McWilliams, J., Molemaker, M., Shchepetkin, A., 2008b. Mesoscale to submesoscale transition in the California Current System. Part iii: Energy balance and flux. *J. Phys. Oceanogr.* 38, 2256–2269.
- Castilla, R., Redondo, J.M., Gamez-Montero, P.J., Babiano, A., 2007. Particle dispersion processes in two-dimensional turbulence: a comparison with 2-d kinematic simulation. *Nonlinear Proc. Geophys.* 14 (2), 139–151.
- Chang, Y., Xu, X., Özgökmen, T., Chassignet, E., Peters, H., Fischer, P., 2005. Comparison of gravity current mixing parameterizations and calibration using a high-resolution 3d nonhydrostatic spectral element model. *Ocean Modell.* 10, 342–368.
- Costa, M., Goldberger, A., Peng, C., 2005. Multiscale entropy analysis of biological signals. *Phys. Rev.* 71, 021906.
- Davis, R., 1985. Drifter observations of coastal currents during CODE. The method and descriptive view. *J. Geophys. Res.* 90, 4741–4755.
- Fischer, P.F., 1997. An overlapping Schwarz method for spectral element solution of the incompressible Navier–Stokes equations. *J. Comput. Phys.* 133, 84–101.
- Fox-Kemper, B., Ferrari, R., Hallberg, R., 2008. Parameterization of mixed-layer eddies. Part i: Theory and diagnosis. *J. Phys. Oceanogr.* 38, 1145–1165.
- Gaspard, P., Wang, X., 1993. Noise, chaos and  $(\epsilon - \tau)$ -entropy per unit time. *Phys. Rep.* 235, 291–343.

- Haller, G., 2002. Lagrangian coherent structures from approximate velocity data. *Phys. Fluids* 14, 1851–1861.
- Haza, A., Özgökmen, T., Griffa, A., Garraffo, Z., Piterbarg, L., 2012. Parameterization of particle transport at submesoscales in the Gulf Stream region using Lagrangian subgridscale models. *Ocean Modell.* 42, 31–49.
- Haza, A., Özgökmen, T., Griffa, A., Molcard, A., Poulain, P., Peggion, G., 2010. Transport properties in small scale coastal flows: relative dispersion from VHF radar measurements in the Gulf of La Spezia. *Ocean Dyn.* 60, 861–882.
- Haza, A.C., Poje, A., Özgökmen, T.M., Martin, P., 2008. Relative dispersion from a high-resolution coastal model of the Adriatic Sea. *Ocean Modell.* 22, 48–65.
- Ilicak, M., Özgökmen, T., Özsoy, E., Fischer, P., 2009. Non-hydrostatic modeling of exchange flows across complex geometries. *Ocean Modell.* 29, 159–175.
- Klein, P., Lapeyre, G., 2009. The oceanic vertical pump induced by mesoscale and submesoscale turbulence. *Annu. Rev. Mar. Sci.* 1, 351–375.
- Koszalka, I., LaCasce, J.H., Orvik, K.A., 2009. Relative dispersion statistics in the Nordic Seas. *J. Mar. Res.* 67, 411–433.
- LaCasce, J., Bower, A., 2000. Relative dispersion in the subsurface North Atlantic. *J. Mar. Res.* 58, 863–894.
- LaCasce, J.H., 2008. Statistics from Lagrangian observations. *Prog. Ocean.* 77 (1), 1–29.
- LaCasce, J.H., Ohlmann, C., 2003. Relative dispersion at the surface of the Gulf of Mexico. *J. Mar. Res.* 61 (3), 285–312.
- Lacorata, G., Aurell, E., Vulpiani, A., 2001. Drifter dispersion in the Adriatic sea: Lagrangian data and chaotic model. *Ann. Geophys.* 19, 121–129.
- Lumpkin, R., Elipot, S., 2010. Surface drifter pair spreading in the North Atlantic. *J. Geophys. Res. Oceans* 115, C12017.
- Lumpkin, R., Pazos, M., 2007. Measuring surface currents with Surface Velocity Program drifters: the instrument, its data, and some recent results. In: Griffa, A., Kirwan, A.D., Mariano, A., Özgökmen, T., Rosby, T. (Eds.), *Lagrangian Analysis and Prediction of Coastal and Ocean Dynamics*, pp. 39–67.
- Maday, Y., Patera, A.T., 1989. Spectral element methods for the Navier–Stokes equations. In: Noor, A.K. (Ed.), *State of the Art Surveys in Computational Mechanics*. ASME, pp. 71–143.
- Mahadevan, A., Tandon, A., 2006. An analysis of mechanisms for submesoscale vertical motion at ocean fronts. *Ocean Modell.* 14, 241–256.
- Mahadevan, A., Tandon, A., Ferrari, R., 2010. Rapid changes in the mixed layer stratification driven by submesoscale instabilities and winds. *J. Geophys. Res.* 115, C03017. <http://dx.doi.org/10.1029/2008JC005203>.
- McWilliams, J., 2008. Fluid dynamics at the margin of rotational control. *Environ. Fluid Mech.* 8, 441–449.
- McWilliams, J.C., 1985. Submesoscale, coherent vortices in the ocean. *Rev. Geophys.* 23 (2), 165–182.
- Müller, P., McWilliams, J., Molemaker, M., 2005. Routes to dissipation in the ocean: the two-dimensional/three-dimensional turbulence conundrum. In: Baumert, H.Z., Simpson, J., Sündermann, J. (Eds.), *Marine Turbulence: Theories, Observations, and Models*. Results of the CARTUM Project. Cambridge University Press, pp. 397–405.
- Ohlmann, J.C., White, P.F., Sybrandy, A.L., Niiler, P.P., 2005. GPS-Cellular drifter technology for coastal observing system. *J. Atmos. Oceanic Technol.* 22, 1381–1388.
- Okubo, A., 1970. Horizontal dispersion of floatable particles in vicinity of velocity singularities such as convergences. *Deep-Sea Res.* 17 (3), 445.
- Ollitrault, M., Gabillet, C., DeVerdiere, A.C., 2005. Open ocean regimes of relative dispersion. *J. Fluid Mech.* 533, 381–407.
- Özgökmen, T., Fischer, P., 2008. On the role of bottom roughness in overflows. *Ocean Modell.* 20, 336–361.
- Özgökmen, T., Fischer, P., in press. CFD application to oceanic mixed layer sampling with Lagrangian platforms. *Int. J. Comp. Fluid. Dyn.* doi:10.1080/10618562.2012.668888.
- Özgökmen, T., Fischer, P., Johns, W., 2006. Product water mass formation by turbulent density currents from a high-order nonhydrostatic spectral element model. *Ocean Modell.* 12, 237–267.
- Özgökmen, T., Iliescu, T., Fischer, P., 2009a. Large eddy simulation of stratified mixing in a three-dimensional lock-exchange system. *Ocean Modell.* 26, 134–155.
- Özgökmen, T., Iliescu, T., Fischer, P., 2009b. Reynolds number dependence of mixing in a lock-exchange system from direct numerical and large eddy simulations. *Ocean Modell.* 30, 190–206.
- Özgökmen, T., Iliescu, T., Fischer, P., Srinivasan, A., Duan, J., 2007. Large eddy simulation of stratified mixing in two-dimensional dam-break problem in a rectangular enclosed domain. *Ocean Modell.* 16, 106–140.
- Özgökmen, T., Poje, A., Fischer, P., Haza, A., 2011. Large eddy simulations of mixed layer instabilities and sampling strategies. *Ocean Modell.* 39, 311–331.
- Özgökmen, T.M., Fischer, P.F., Duan, J., Iliescu, T., 2004a. Three-dimensional turbulent bottom density currents from a high-order nonhydrostatic spectral element model. *J. Phys. Oceanogr.* 34 (9), 2006–2026.
- Özgökmen, T.M., Fischer, P.F., Duan, J., Iliescu, T., 2004b. Entrainment in bottom gravity currents over complex topography from three-dimensional nonhydrostatic simulations. *Geophys. Res. Lett.* 31, L13212. <http://dx.doi.org/10.1029/2004GL020186>.
- Patera, A., 1984. A spectral element method for fluid dynamics; laminar flow in a channel expansion. *J. Comput. Phys.* 54, 468–488.
- Pattanayak, A., 2001. Characterizing the metastable balance between chaos and diffusion. *Physica D* 148, 1–19.
- Pierrehumbert, R., 1994. Tracer microstructure in the large-eddy dominated regime. *Chaos Solitons Fract.* 4, 1091–1110.
- Poje, A., Haza, A., Özgökmen, T., Magaldi, M., Garraffo, Z., 2010. Resolution dependent relative dispersion statistics in a hierarchy of ocean models. *Ocean Modell.* 31, 36–50.
- Prince, P.J., Dormand, J.R., 1981. High order embedded Runge–Kutta formulae. *J. Comput. Appl. Math.* 7 (1).
- Richardson, L.F., 1926. Atmospheric diffusion shown on a distance-neighbour graph. *Proc. Royal Soc. Lond.: Ser. A* 110 (756), 709–737.
- Schroeder, K., Haza, A.C., Griffa, A., Özgökmen, T.M., Poulain, P., Gerin, R., Peggion, G., Rixen, M., 2011. Relative dispersion in the liguro-provençal basin: from submesoscale to mesoscale. *Deep Sea Res.* 1 58, 861–882.
- Shadden, S., Lekien, F., Marsden, J., 2005. Definition and properties of Lagrangian coherent structures from finite-time Lyapunov exponents in two-dimensional aperiodic flows. *Physica D* 212 (3–4), 271–304.
- Sundaram, B., Poje, A., Pattanayak, A., 2009. Persistent patterns and multifractality in fluid mixing. *Phys. Rev. E* 79, 066202.
- Sundermeyer, M., Ledwell, J., 2001. Lateral dispersion over the continental shelf: analysis of dye release experiments. *J. Geophys. Res.* 106, 9603–9621.
- Thomas, L., Tandon, A., Mahadevan, A., 2008. Submesoscale processes and dynamics. *Ocean modeling in an Eddying Regime*, edited by M. Hecht and H. Hasume. *Geophys. Monogr.* 177, 17–38.
- Titaut, O., Brankart, J.-M., Verron, J., 2011. On the use of finite-time Lyapunov exponents and vectors for direct assimilation of tracer images in ocean models. *Tellus* 63A, 1038–1051.
- Weiss, J., 1991. The dynamics of enstrophy transfer in 2-dimensional hydrodynamics. *Physica D* 48 (2–3), 273–294.
- Xu, X., Chang, Y., Peters, H., Özgökmen, T., Chassignet, E., 2006. Parameterization of gravity current entrainment for ocean circulation models using a high-order 3d nonhydrostatic spectral element model. *Ocean Modell.* 14, 19–44.